ABSTRACT

Title of Thesis: AERO DATABASE DEVELOPMENT AND TWO-DIMENSIONAL HYPERSONIC TRAJECTORY OPTIMIZATION FOR THE HIGH-SPEED ARMY REFERENCE VEHICLE

Brendan James
Master of Science, 2023

Thesis Directed by: Dr. Christoph Brehm
Department of Aerospace Engineering

Dr. Johan Larsson
Department of Mechanical Engineering

Steady-flow inviscid and simulations of the High-Speed Army Reference Vehicle geometry were performed within the CHAMPS solver framework at Mach numbers of 4, 6, and 8, and an integrated streamline method was used to apply viscous corrections for Reynolds numbers up to 2×10^8. For each flow Mach, angle of attack sweeps from -10° to +10° were used to determine baseline drag, lift, and moment coefficient alpha dependencies. Coefficient values were then interpolated across Mach, alpha, and Reynolds number parameter spaces to construct an aerodynamic force coefficient database for use in two-dimensional flight simulation and trajectory optimization. By simulating flight with a maximum lift-to-drag control input, sample trajectories for determining maximum vehicle range were produced. A proportional-navigation controller was implemented which allowed for the targeting of specific trajectory altitudes. The PN controller

and simulation schemes were then utilized in genetic-algorithm optimization to produce trajectory profiles for achieving minimum time-to-target for gliding flight in standard atmospheric conditions. Over the examined range of initial altitudes, Mach numbers, and release angles, the fastest trajectories were consistently shown to be those which achieved or maintained stratospheric altitudes and consequently benefited from significantly reduced drag before performing a nose-over maneuver for an accurate ground strike.

AERO DATABASE DEVELOPMENT AND TWO-DIMENSIONAL HYPERSONIC TRAJECTORY OPTIMIZATION FOR THE HIGH-SPEED ARMY REFERENCE VEHICLE

by

Brendan James

Thesis submitted to the Faculty of the Graduate School of the
University of Maryland, College Park in partial fulfillment
of the requirements for the degree of
Master of Science
2023

Advisory Committee:
Professor Christoph Brehm, Chair/Advisor
Professor Johan Larsson, Co-Advisor
Professor James Baeder

Acknowledgments

Firstly, I would like to thank my primary advisor, Dr. Christoph Brehm, and my co-advisor in the hypersonic waverider project, Dr. Johan Larsson. Being given the opportunity to continue my studies in aerospace engineering at the University of Maryland has been an incredible experience, and the wonderful insight into higher-level research as well as the academic guidance that they have provided during my time here have been invaluable. This effort would simply not have been possible without their assistance.

Thanks are also due to Dr. James Baeder, who agreed to participate in the advisory committee of my thesis defense. His far-reaching knowledge and passion for teaching the CFD courses were immediately evident even in the one semester that I spent studying with him. I thoroughly enjoyed his teaching this fall and pride myself in being one of the only 2023 Naval Academy aerospace graduates to have taken a CFD course at the graduate level, especially from a professor as experienced in the subject as Dr. Baeder.

I am greatly indebted to the wonderful students in Dr. Brehm's research lab for their help in operating the CFD solver, solving research problems, and critiquing research presentation material. Sean Dungan, Sparsh Ganju, and in particular William van Noordt were incredibly helpful and supportive throughout my limited time at UMD. I wish them all the best in their remaining studies and the start of their careers.

I owe an immense amount of thanks to the staff and faculty of the United States Naval

Academy. Thank you, Dr. Gabriel Karpouzian, for an unforgettably thorough dive into the world of aerodynamics. Thank you to Col. Scott Davids and CAPT Scott Drayton, who taught with indelible humour and set a gold standard for midshipmen to emulate as future officers. Thank you LCDR Michael McClean for your guidance in securing my spot as a Student Naval Aviator. And thank you especially CAPT Robert Niewoehner, who made the Academy's aerospace program like no other, who reignited my love of the subject, and who tolerated many a diving catch.

To my parents, Arlene and Michael, everything I pursue stems from your example. I love and cherish you both, and hope that an assignment to Texas is in my future so that I can visit more than twice a year. Go Rangers, and wreck 'em Tech. Without the support and love of my paternal grandfather, Sonny, and that of my maternal grandmother, Val (Nani), I would not be where I am today. Nani, I know that I will never have as big a fan as you as long as I live. To my extended family, Norma, Ray, Fiona, Kylie, Andrew, Chantal, Rob, and Laura: no words can describe the lifetime of memories you have and continue to provide me. Lachlan and Cameron: fly high, and listen to your Mum and Ma. To my sister, Phoebe, you are the most important person in my life, and I hope to one day be half as cool as you are.

In my service to the country, I follow in the footsteps of my maternal grandfather and step-grandfather, John and Howard. Your examples left a tremendous impact on me, and I wish that you were both still here today to follow me on my journey.

Finally, I would be remiss not to thank David Lown, the jazz director of Carroll Senior High School, for showing me how to actually give something my entire effort.

Table of Contents

List of Tables

List of Figures

Chapter 1: Introduction

A key challenge in the design of any air-vehicle platform is the characterization of its aerodynamic properties across a wide range of flight conditions [1]. The necessary scope and fidelity of the aerodynamic characterization is highly dependant on vehicle mission and configuration. While it is not always necessary or cost-effective to generate an exhaustive aerodynamic database for a given vehicle, an accurate and adequately complete database can in many cases be enormously helpful in helping to inform design decisions, performing accurate flight simulations, and optimizing mission and flight profiles.

Today, aerodynamic database analysis is used as an effective time and cost-saving measure over more brute-force approaches to platform testing. These benefits are compounded when database development can be performed with CFD simulations rather than physical testing, especially when considering the added complexities of supersonic and hypersonic flight. While the aerodynamic characterization of strictly subsonic vehicles can be accomplished in a relatively straightforward manner, variability in aerodynamic forces introduced by supersonic and hypersonic flight phenomena create the need for a much wider scope of aerodynamic data. The strength, orientation, and transitory nature of shocks at high flight Mach numbers can significantly affect the resulting aerodynamic forces experienced by a given vehicle geometry. These phenomena are further compounded in viscous analysis by the introduction of friction and significantly more relevant

heating effects, particularly in the flow boundary layer, and by the inclusion of high-temperature dissociation and other real gas effects [2].

The motivation of this work is to develop a two-dimensional flight simulation code to investigate the characteristics of time-minimized optimal flight trajectories for given initial flight conditions and target distances. Additionally, the maximum range capabilities of the chosen vehicle are also investigated based off of a max lift-to-drag flight profile. In order to accomplish this, an aerodynamic force database is developed based off of inviscid CFD simulations of the geometry, as well as integrated boundary-layer viscous corrections to the inviscid simulations. The geometry selected for analysis is the High-Speed Army Reference Vehicle (HARV), developed jointly by the DEVCOM Army Research Laboratory and Texas A&M University System Bush Combat Development Complex [3].

1.1 Historical Aero Database Uses

While the usefulness of an aerodynamic database in assessing vehicle aerodynamic performance has always been evident, the ability to construct them with reliable accuracy has not always been attainable, and many design efforts are subjected to program resource constraints. Historically, the use of wind tunnel test data has been a necessary starting point, but the approach carries with it the difficulties associated with any wind tunnel testing plan, including access to properly suited tunnel facilities, construction of appropriately sized and accurate test models, and the potential for a significant time and monetary cost [1]. Hypersonic testing introduces additional challenges to these efforts, as the conditions necessary to simulate hypersonic flight are not easy to create, and can often only be achieved on very short timescales. With the exponential rise in processor

power in the latter half of the 20th century, computers began to play a much more important role in database construction, but their use was focused mainly on implementing predictive algorithms which interpolate and extrapolate existing physical test data, rather than full or partial-flowfield CFD simulations.

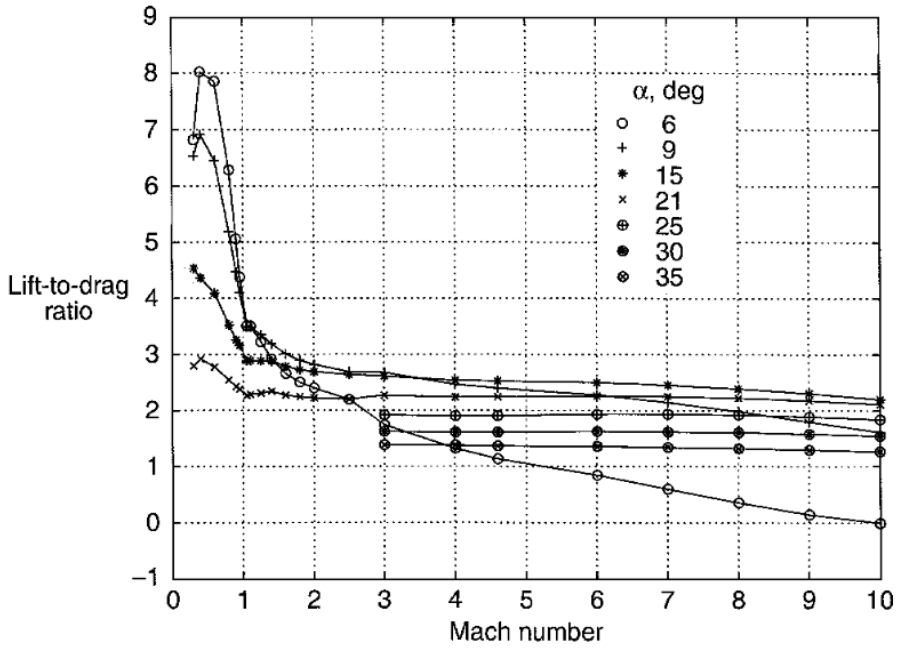

Figure 1.1: X-34 Lift/Drag Ratio Database from from Ref. 4

An example of a predictive algorithm-based database is the the Aerodynamic Preliminary Analysis System (APAS) used in the building of a database for NASA's Orbital Science X-34 project, shown in Figure 1.1 [4]. In this implementation, wind tunnel data was used whenever it was available, and APAS predictions were used in the remaining angle of attack/Mach parameter. While this provided a computationally efficient database, implementation of later wind tunnel data showed the algorithm to lack accuracy at some conditions, especially if it was not fed a sufficient amount of test data near a particular flight condition.

Gradually, sufficiently high-fidelity CFD simulations became a valid option for obtaining

necessary test results for building a database. Usually, these results are supplemented by wind tunnel or full-scale flight test data whenever available, but the rapidity of changing conditions in CFD simulations compared to physical testing makes it especially viable at the outset of a platform design process [8].

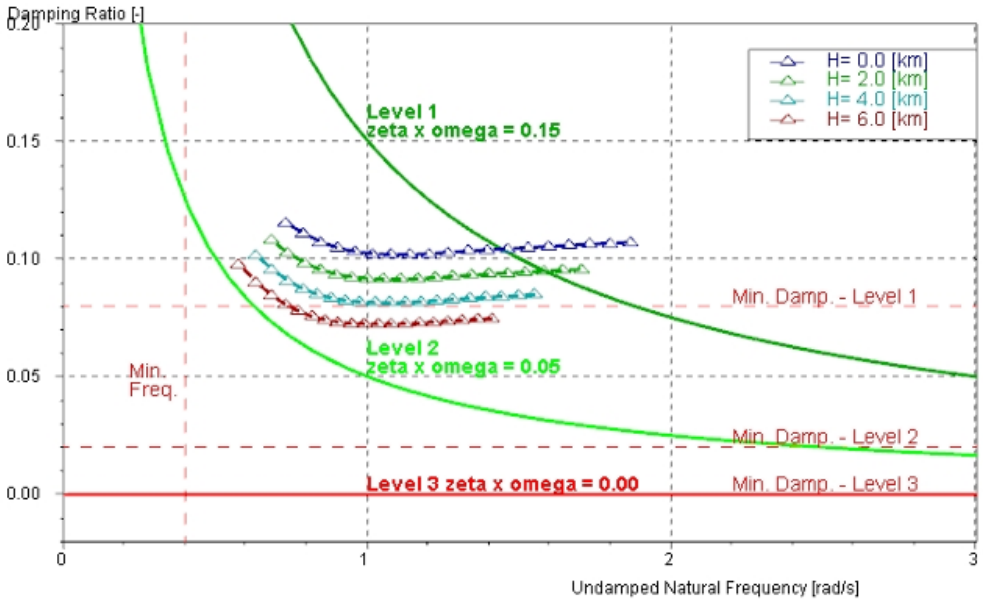

Figure 1.2: Dutch Roll damping ratio data obtained from CFD-supplied aero database in Ref. 7

The uses of databases in general has also evolved from simply estimating general aerodynamic properties of a vehicle across a flight envelope to being used to obtain in-depth analysis of the performance, stability, and control characteristics of pre-production aircraft, which grants insights into even more areas of the aircraft's design [7]. An example is given in Figure 1.2, which depicts dynamic stability simulation results in the dutch roll mode for a CFD-derived aerodatabase. A final advantage of databases is noted for platforms which were not designed to be recoverable, and which are therefore more difficult to obtain full-scale flight test data for, which is applicable for high-speed payload-oriented designs such as the HARV [6]. This effort will aim to reinforce the use of aerodynamic databases as a valid design and performance analysis

tool. It will further aim to demonstrate that even in the wide-ranging atmospheric and flight conditions encountered by a hypersonic air vehicle, a database can be developed for relatively low computational cost, which can provide useful insight into later-stage design phases including trajectory optimization and determining maximum range.

1.2 Hypersonic Trajectory Optimization

With the prospect of hypersonic high-lift flight applications in military and civilian sectors becoming increasingly real, significant effort has been made to search for ways in which to solve the highly non-linear coupled problems of optimizing vehicle trajectory for parameters such as minimizing point-to-point flight time, maximizing terminal velocity, and reducing peak heating to a structurally acceptable limit. The main benefit of high-lift hypersonic vehicles is their ability to maintain higher altitudes for longer during a given maneuver, which can lead to significant reductions in drag and heating.

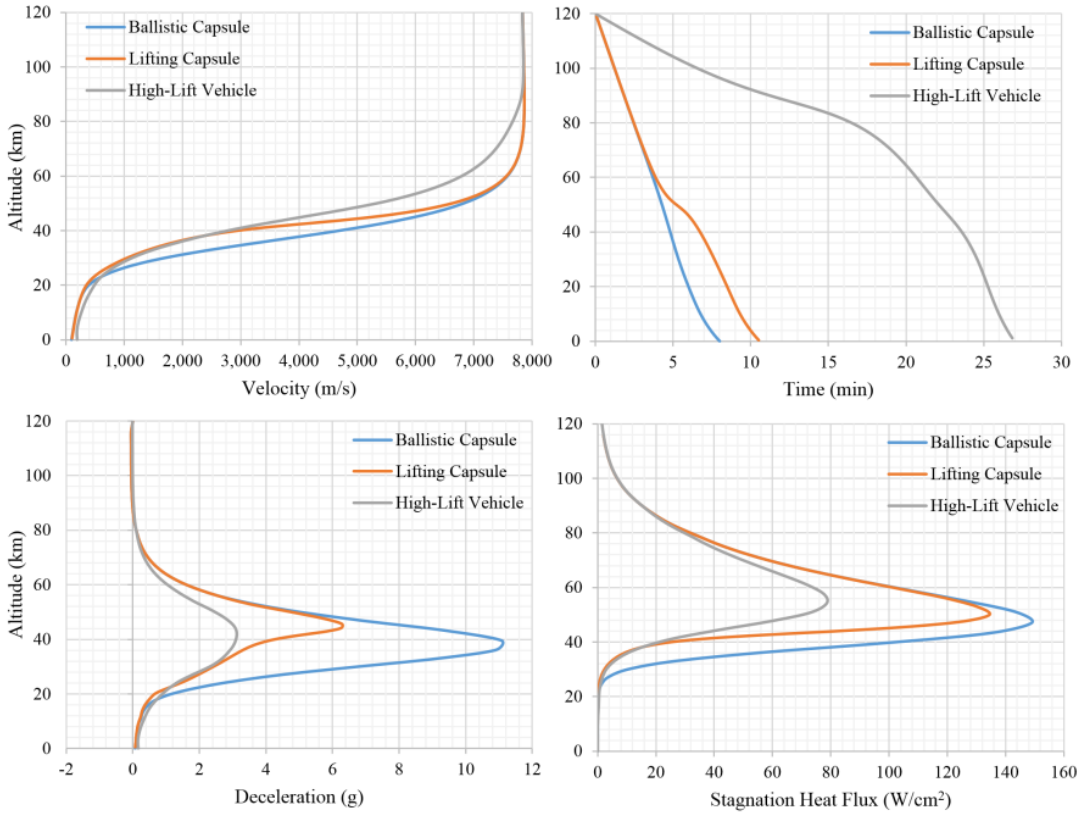

Figure 1.3: Comparison of reentry profiles for ballistic and lifting vehicles from Ref. 19

An example of this benefit is given Figure 1.3. These trajectory profiles compare the velocity, time of flight, acceleration, and heat flux of a baseline ballistic capsule, a lifting capsule, and a specialized high-lift hypersonic vehicle. The high-lift vehicle is capable of maintaining a higher altitude for much longer than the other designs, and consequently experiences a significantly reduced peak deceleration and heat flux. While the given trajectory is one which utilizes the high lift capability of the vehicle to minimize drag and heating, it does so at the expense of a very long flight time. This reinforces the notion that trajectories are highly mission and vehicle dependant.

Due to the complexity and range of flight conditions encountered by high-altitude hypersonic vehicles, several approaches have been explored to solve for optimal trajectories, with some efforts choosing to emphasize linear relaxation techniques to provide convergence [11]. Other

efforts explore more computationally efficient but less definitive indirect solutions [20]. Still further approaches have incorporated the use of deep-learning schema and genetic algorithms to seek an iterative convergence to optimal solutions [5]. Control logic is also necessarily a factor in determining viable and optimal trajectories for a given mission, as most currently proposed hypersonic vehicle designs will be unmanned [15] [16]. This work will concentrate mainly on answering the question of characterizing optimal profiles during a hypothetical glide-to-target phase of flight for the HARV, incorporating both active vehicle-controller logic and the use of genetic algorithms in the optimization process.

1.3 High-speed Army Reference Vehicle

Schematics for the HARV were published by DEVCOM Army Research Laboratory in August 2022 [3]. The goal of the project was to publish a semi-modular reference geometry for use in academic research and scientific discourse. It features relevant hypersonic-flow design elements without being specific to ongoing development projects. Two frontal cone designs were given, one being a cone with a half-angle of 5°, and the other being a Von Kármán ogive. Additionally, equal-spaced three and four-fin configurations were proposed for the rear section. Control surfaces are not explicitly described in the published schematics, and are not modeled here.

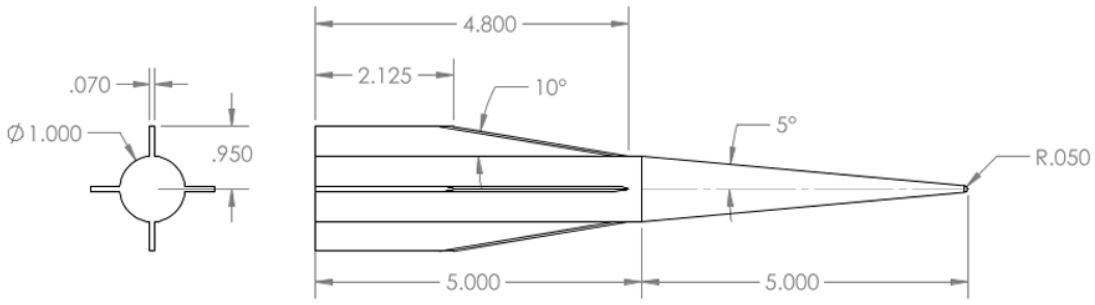

Figure 1.4: HARV Schematics, units of calibers, Ref. 3

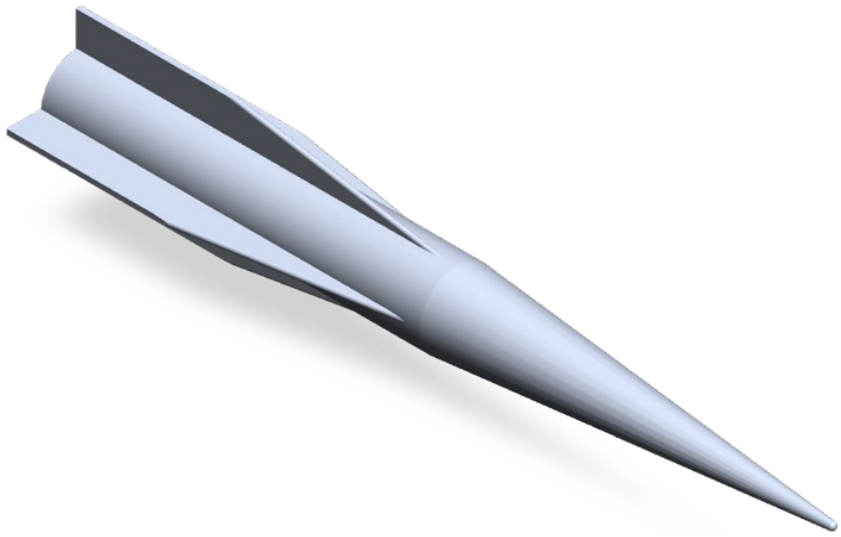

Figure 1.5: HARV rendering, conical four-fin configuration Ref. 3

For this analysis, the cone-tipped, four-fin configuration was selected for analysis. The dimensions in units of calibers (ratio to the base diameter) are shown in Figure 1.4 and a rendering of the model is shown in Figure 1.5. The body length is 10 calibers (as with all HARV configurations), and the four symmetrically-arranged fins have a root-to-tip chord length of 4.8 calibers at the body surface and 2.125 calibers at the fin edge.

Chapter 2: Methodology

2.1 Introduction

To construct the HARV aero database, simulations were performed using the in-house CHAMPS (Cartesian High-order Adaptive MultiPhysics Solver) [12]. Flow outputs were fed to a post-processing tool to obtain raw aerodynamic force data, which were then used in MATLAB to interpolate and extrapolate from the measured data across the flight state parameter space. Once the database had been fully constructed, they were used as the force coefficient basis to write two-dimensional trajectory simulation and optimization scripts in MATLAB.

2.2 CHAMPS Simulations

2.2.1 Inviscid Simulations

The first series of simulations performed were steady and inviscid, for which the governing equations are the compressible Euler equations. CHAMPS, as the name suggests, is capable of automatically refining a Cartesian grid around body geometry, as well as providing added fidelity near the most important flow features, namely the conical and fin-produced shocks. Examining only alpha relationships to aerodynamic forces meant that a half-geometry could be used to cut down on solver runtime.

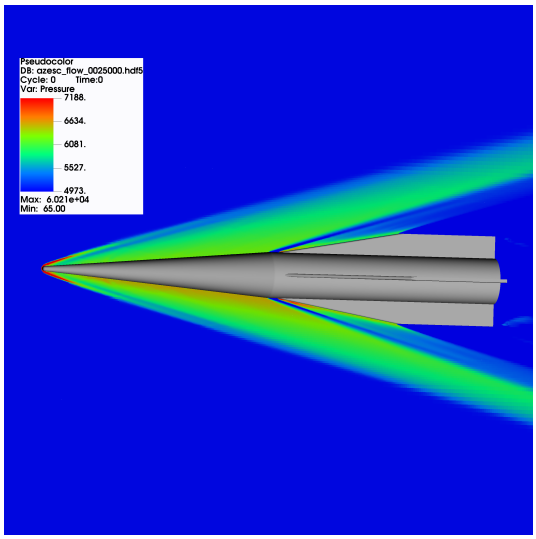

(a) $\alpha = 0.5°$

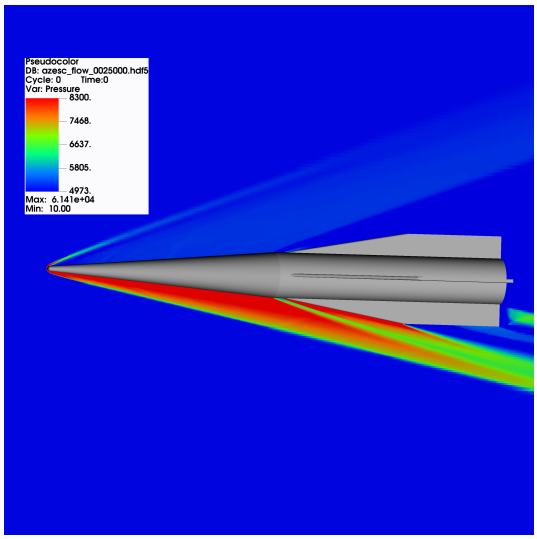

(b) $\alpha = 5.5°$

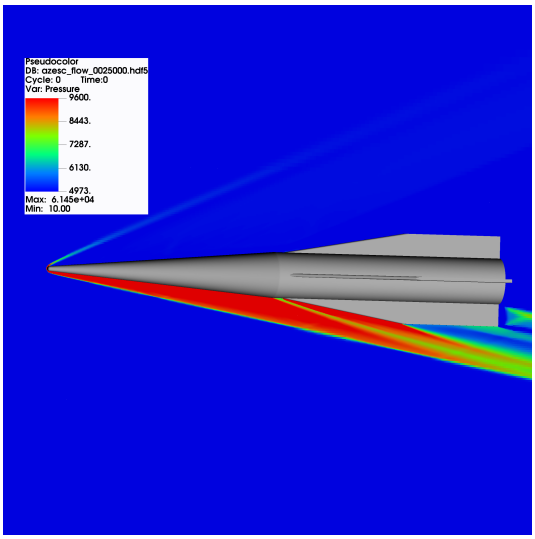

(c) $\alpha = 8.5°$

Figure 2.1: Mach 4 inviscid pressure visualizations at low, moderate, and high angles of attack

The scheme used by CHAMPS to solve for inviscid fluxes was a 5th-order WENO scheme. The HARV was modelled with a length of 0.5 meters, and was positioned with the tip of the cone at the origin of the Cartesian coordinate system, with its longitudinal axis along the positive x direction, the lateral axis in the z direction, and the vertical axis in the y direction. The grid limits were set in the x-direction from -0.1 m (slightly forward of the nose) to +0.9 m (aft of the base to properly capture shocks exiting the flowfield), in the y direction from -0.45 to +0.45 m,

and in the z direction from 0 m (bisection of the geometry) to 0.35m. After a grid convergence study, resolution settings were such that the smallest solver-refined grid spacing was on the order of 1×10^{-3} m in each dimension.

Mach 4 pressure visualizations at the geometry midline are shown in Figure 2.1 Several key flow structures are visible including the outer conical shock. The strength of the primary conical shock near the bottom of the vehicle and the resulting pressure jump increased with an increase in angle of attack. A small area of expansion is seen near the joining of the conical nose and the cylindrical aft body, which are succeeded by the smaller shocks produced by the interface of the fins with the body. The flowfield above the body exhibits a significantly reduced overall pressure at higher angles of attack, owing to expansion around the geometry surface and its position in the aerodynamic 'shadow' of the HARV.

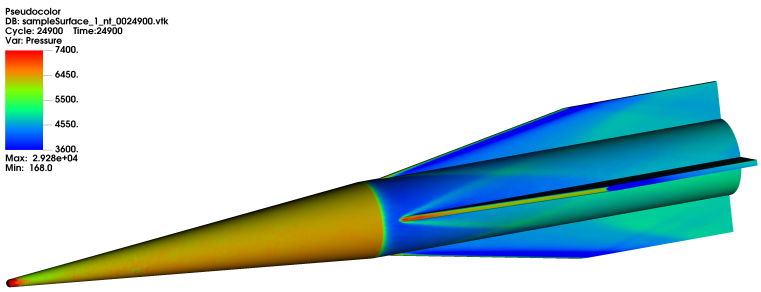

Figure 2.2: Inviscid surface pressure of the HARV at Mach 4, $\alpha = 8.5°$

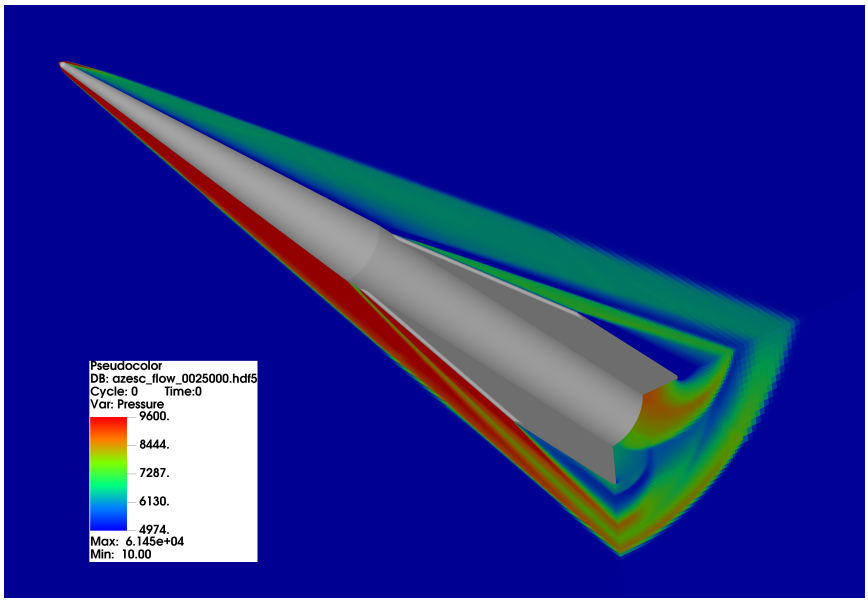

Figure 2.3: Inviscid three-slice pressure visualization ath Mach 4, $\alpha = 8.5°$

Figures 2.2 and 2.3 depict the surface pressure and a three-slice pressure visualization of the Mach 4, $\alpha = 8.5°$ case, respectively. The surface pressure depiction shows the effect of the nose-body interface on flow pressure clearly, as the expanded flow aft of the interface exhibits a much lower pressure than that of the cone immediately before it. This pressure is increased further along the body as a result of secondary, fin-produced shock interactions. In the three-view depiction, the shape and relative intensities of the three-dimensional shocks can be more easily seen towards the rear of the HARV. The high pressure of the flow under the fin most directly exposed to the free stream is also visible here.

Table 2.1: Aerodynamic database parameter ranges

Parameter	Min	Max
α (deg)	-10	+10
Mach	2	10
Re	100	2×10^8

Table 2.3 depicts the overall parameter space for the database. Reynolds number was

relevant only to the viscous database, discussed in the next section. For the Mach 4 cases, angle of attack was iterated in half-degree increments from -10 to +10 degrees. For the Mach 6 and Mach 8 cases, the increment was increased to one degree, over the same total range.

As the flow near the base of the HARV would in reality be almost entirely separated, the predicted pressure near that area and resulting aerodynamic force outputs were considered to be non-physical. To determine more accurate force readings, pressure data at each geometry face was extracted and integrated across the vehicle surface via a post-processing script written by William van Noordt[1]. At the base, a pressure correction proposed by Maxwell [19] was used, which assumed that base pressure was equal to the free-stream pressure divided by the freestream Mach number. Force and moment measurements were then normalized by the base area S, free-stream dynamic pressure, and the center of mass (for moments only) in order to find lift, drag, and moment coefficients for each condition.

2.2.2 Viscous Simulations

To incorporate viscous effects into the database without having to perform fully viscous simulation cases, an integrated streamline method was used to estimate the viscous drag and effect on the boundary layer. To account for a large range in expected atmospheric densities and velocities, surface pressures and viscous drag were calculated using this method at Reynolds numbers ranging from an extreme-low 100 to a maximum of 2×10^8. The same post-processing point-integrated pressure treatment and Maxwell base pressure estimation was used as in the inviscid cases to determine aerodynamic forces and coefficients.

Following the compilation of drag, lift, and moment coefficient values for all flow cases,

[1]Ph.D candidate, Oxford University

MATLAB was used to interpolate across the parameter spaces of angle of attack, Mach, and Reynolds number. A spline interpolation was used initially to extrapolate coefficients across the total Mach range of 2 to 10. Then, an alpha interpolation was performed in order to increase alpha-dependent resolution. A cubic interpolation was used in this step in order to more closely mimic the physical force-alpha correlation. Extrapolation beyond angles of attack of positive or negative ten degrees was not performed as this was the maximum range considered for use in the trajectory simulations. Finally, for the viscous data, interpolations were performed across the Reynolds number space. Database coefficient values were stored at a discretization of 0.01 Mach, 0.1° α , and Re 1×10^6, in order to simplify the use of database values in the trajectory simulation code.

2.3 Two-Dimensional Trajectory Simulation

The following sections outline the development of a two-dimensional, cartesian coordinate gliding flight simulator for the HARV, and the use of genetic algorithms in optimizing flight paths for minimum-time trajectories.

2.3.1 Equations of Motion

Figure 2.4 provides a visualization of the two-dimensional motion variables used in HARV trajectory simulations. α represents the angle of attack, or the relative angle between the free-stream velocity vector and the HARV chord line (taken as simply the longitudinal axis), and γ is the flight path angle, or the angle between the velocity vector and the local horizon. From first principles, the two-dimensional equations of motion, decomposed into x and y components, are

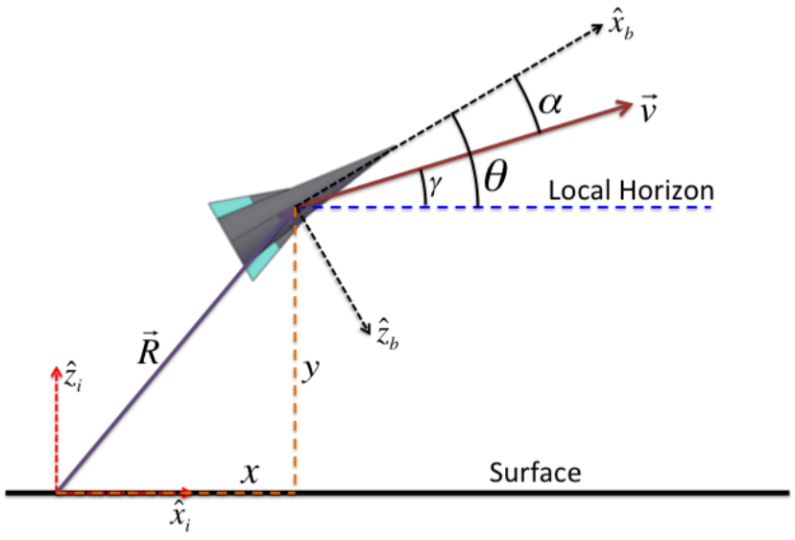

Figure 2.4: Depiction of two-dimensional motion variables adapted from [21]

obtained from Newton's second law in the form

$$\ddot{y} = \frac{\vec{F}_{net,y}}{m} \tag{2.1}$$

$$\ddot{x} = \frac{\vec{F}_{net,x}}{m} \tag{2.2}$$

To determine the total vector sum of all forces in each coordinate direction, aerodynamic forces are first considered with respect to the free-stream reference frame. This is defined by the velocity vector $\vec{v}$ in Figure 2.4. The normal and tangential accelerations in the free-stream reference frame are

$$L' = \frac{1}{2m}\rho_\infty U_\infty^2 C_L(M, \alpha, Re)S, \quad \text{and} \tag{2.3}$$

$$D' = \frac{1}{2m}\rho_\infty U_\infty^2 C_D(M, \alpha, Re)S, \tag{2.4}$$

where ρ_∞, U_∞, m and S are free-stream density, free-stream velocity, vehicle mass, and base

area, respectively. These accelerations are then resolved into the inertial reference frame in the following way, with the addition of gravitational acceleration in the y direction:

$$\ddot{y} = L' \cos\theta - D' \sin\theta - g, \text{ and} \tag{2.5}$$

$$\ddot{x} = -L' \sin\theta - D' \cos\theta, \tag{2.6}$$

where θ is the flight path angle relative to the positive x direction. This derivation supplies us with the non-linear ordinary differential equations for each coordinate with respect to time that will be used in all following HARV flight simulations. The standard U.S. atmosphere model was used for all simulations.

2.3.2 Time Integration Methods

Two main time integration schemes were implemented for the HARV flight path simulations. The first was a forward Euler scheme, expressed succinctly as

$$u_{n+1} = u_n + h u'_n \tag{2.7}$$

Where h represents the timestep, n represents the current time level and $n+1$ the subsequent time level. As the differential equation for position with respect to time was second order, this step was performed twice at each time step, with u' representing the known acceleration and predicted velocity in each respective step. Though exceedingly simple to code and relatively fast at performing simulations, the scheme was known to be $\mathcal{O}(\Delta t)$ accurate, and has an inherent stability restriction on maximum timestep. Thus, it relied on an adequately small timestep

selection in order to remain numerically stable and produce reasonably accurate results [22]. In order to improve time and spatial accuracy, as well as allow for a larger timestep, a Runge-Kutta (RK) scheme was later implemented in the simulation code. The steps in the classical 4th-order RK scheme is given below in predictor-corrector notation.

$$\hat{u}_{n+1/2} = u_n + \frac{1}{2}hu'_n \tag{2.8}$$

$$\tilde{u}_{n+1/2} = u_n + \frac{1}{2}h\hat{u'}_{n+1/2} \tag{2.9}$$

$$\overline{u}_{n+1} = u_n + h\tilde{u'}_{n+1/2} \tag{2.10}$$

$$u_{n+1} = u_n + \frac{1}{2}h[u'_n + 2(\hat{u'}_{n+1/2} + \tilde{u'}_{n+1/2}) + \overline{u'}_{n+1}] \tag{2.11}$$

This method computes several intermediate steps for each timestep before combining them in a weighted linear term to predict the value at the next time level. It is $\mathcal{O}(\Delta t^4)$ accurate. In MATLAB, the integrated ode45 function was used, which is based on 4th and 5th order Runge-Kutta methods [23]. The velocity and position for each coordinate direction could be rewritten as a coupled set of first-order differential equations and solved in one pass by ode45, though it was still necessary to use a relatively small timestep in order to allow for the continual updating of force coefficients at each step pulled from the HARV database.

To validate the accuracy of each method in time and space, a zero drag parabolic trajectory case was ran, with an initial velocity of 1,020.9 m/s (Mach 3 at sea level) and a launch angle of $45°$, shown in Figure 2.5. Table 2.2 summarizes the error compared to the analytical solution and runtime results.

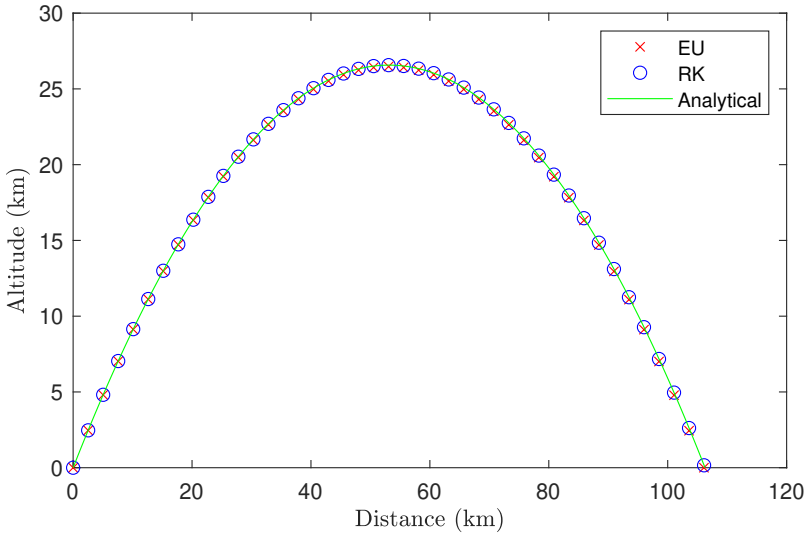

Figure 2.5: Parabolic, zero-drag trajectory validation case

Table 2.2: Scheme validation case results

Scheme	Δt (s)	$\lvert Er_x \rvert$ (m)	$\%Er_x$	$\%Er_t$	Runtime (ms)
EU	0.25	180.2	0.170	0.170	62.9
ode45	0.25	0.0320	3.02×10^{-5}	9.68×10^{-5}	160.0
ode45	0.75	0.5692	5.37×10^{-4}	1.57×10^{-4}	53.7

Although the Euler scheme was considerably faster at running the case with the smaller timestep, the increase in error for both time and space was considerable. Though a few tenths of a percentage of error seems small, it translates to hundreds of meters at the scales present in hypersonic trajectory analysis, where the end point can be hundreds or thousands of kilometers away from the launch point. When the time step was increased to 0.75 seconds in the ode45 scheme, accuracy was preserved while runtime was reduced to below that of the initial Euler simulation. For these reasons, the ode45 implementation was used in almost all subsequent trajectory analysis. Though the timestep could theoretically be increased even further to reduce computational time while maintaining stability and accuracy, this approach led to some errors in the optimization cases due to control-point overshoot, so timestep was kept in the 0.75-1 second

range.

2.4 Trajectory Optimization

2.4.1 Proportional Navigation Controller

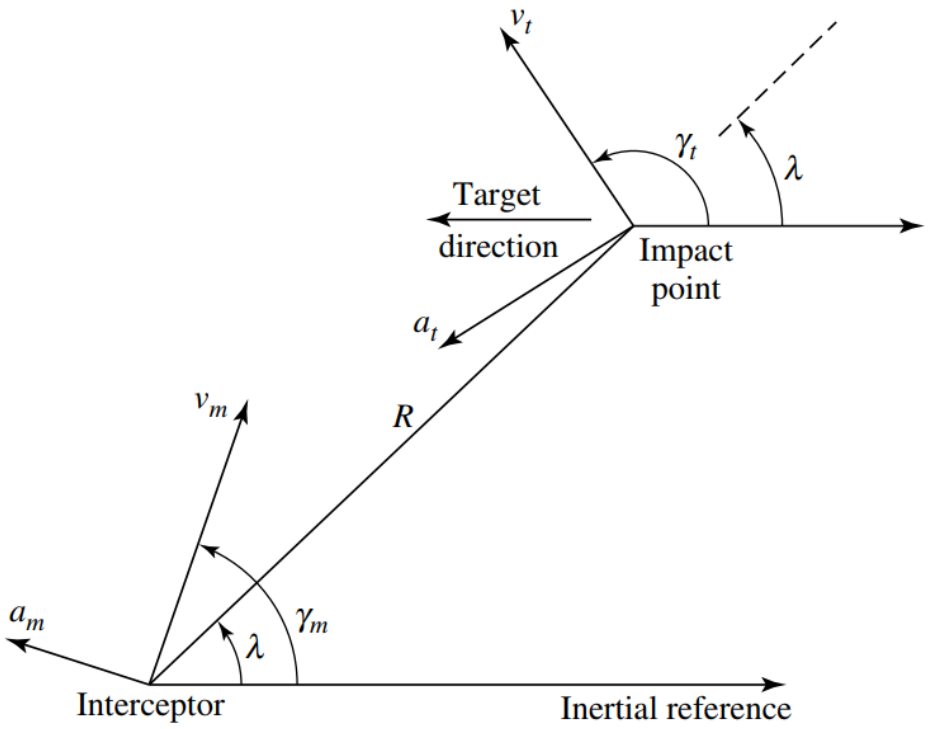

Figure 2.6: 2-D proportional navigation controller geometry

In order to allow for the targeting of specific points along a given trajectory, a proportional-navigation (PN) controller was implemented for use in the simulation. A two-dimensional schematic of the proportional navigation controller is given in Figure 2.6 The mathematical expression of the controller logic is

$$a_n = NV_c(\frac{d\lambda}{dt}), \tag{2.12}$$

where a_n is the commanded normal acceleration, N is the dimensionless navigation constant,

V_c is the closing velocity (the rate of change of the straight line distance between the missile and target, $\frac{dR}{dt}$), and λ is the line-of-sight (LOS) angle between the missile and target, referenced to inertial space. Essentially, the controller seeks to arrest any detected rate of change between the line of sight angle by commanding a velocity-scaled normal acceleration in the appropriate direction. The navigation constant is somewhat arbitrary, but a value of 3 is used in this case, which is suitable for stationary targets [14] [13]. Once the commanded normal acceleration is found, it can be used to solve for the necessary lift coefficient given the current flight condition:

$$C_L = \frac{m(a_n + g)}{Sq_\infty} \tag{2.13}$$

As implemented in the simulation code, this coefficient is searched for in the database for each timestep, and a maximum α=-10 or +10 degrees is used if the commanded lift coefficient exceeds those available at a given Mach and Reynolds number.

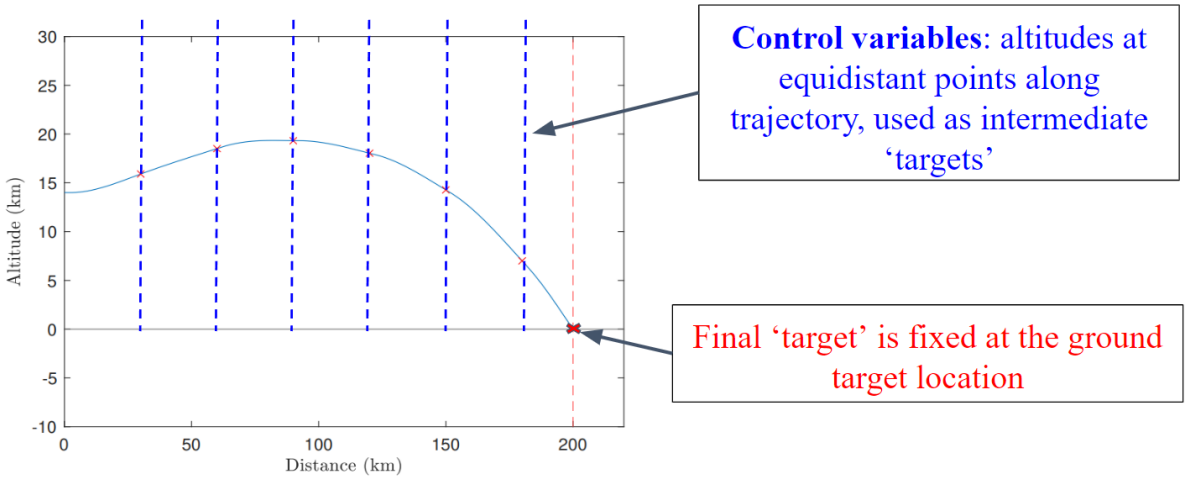

Figure 2.7: Proportional navigation control point visualization

The immediate benefit of using this controller method is that it allowed for the use of specific altitude/downrange points as control variables during the optimization process, which

maximized the ability of the optimization algorithm to extract meaningful solutions based on actual atmospheric interactions, rather than the more crude method of controlling alpha directly. A visualization of the control point setup is shown in Figure 2.7. The bolded dashed lines along the trajectory represent the equidistant locations at which an altitude can be defined for the HARV to target using the PN controller. As the HARV passes one such target, it automatically switches to using the subsequent control point as the next control point. For each trajectory, the final control point is always set as the ground target, such that the HARV will perform a target-seeking ground strike once the penultimate control point has been passed, provided that it has enough control authority and energy remaining.

2.4.2 Genetic Algorithm Optimization

Genetic algorithms are based on the principles of evolution. They evaluate a wide population of guess 'individuals' are evaluated against an objective function, before retaining a selection of the 'most fit' population members, and then 'mutating' them through a combination of random-number based alterations or crossover functions with other elite individuals, which are then evaluated in the next 'generation' [24] [25]. With correct formulation, guesses will steadily improve in fitness, but convergence to a global optimal is not guaranteed. They are a relatively inefficient optimization algorithm, and require fine-tuning in order to be able to solve optimization problems quickly. However, they are non-deterministic, meaning that they do not measure any sort of gradient with respect to the objective function. The benefit of this characteristic is that with a sufficiently long runtime, genetic algorithms may find solutions which score better than a local objective function minimum which would have otherwise 'fooled' a deterministic method.

On the other hand, the required runtime can be quite significant depending on problem setup and user-controlled settings, and convergence to a global or even local minimum is never guaranteed. A previous use of GA-optimization for this type of problem is given in Reference [5].

The defined problem of this research is to investigate characteristics of trajectories to a ground target which minimize time of flight. The objective function formulated for this research is given as

$$J_{min} = wt_{flight} + (1 - w)(|x_{impact} - x_{target}|)^2, \tag{2.14}$$

where w is the relative weight of the time-to-target and the accuracy of the strike. The weight term was chosen to be relatively high ($\sim$0.9) in most cases to favor the effect of minimizing time of flight, as the miss distance term functioned more to penalize inaccurate strike trajectories. This formulation ensures that trajectories which are both fast and accurate will score well, while wildly penalizing those trajectories which minimize time but are completely inaccurate. The PN controller was particularly useful when combined with this objective function, as it ensured that many solutions would reach the target with considerable accuracy, but only those that did so quickly would be considered as elite, and survive to produce even faster solutions.

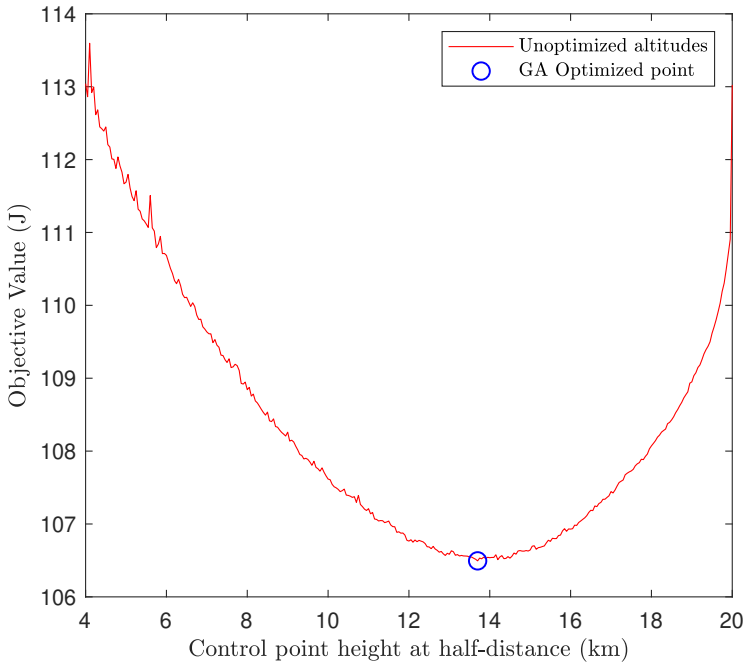

Figure 2.8: GA-validation case for one control point, h_{init}=8 km, M = 7.

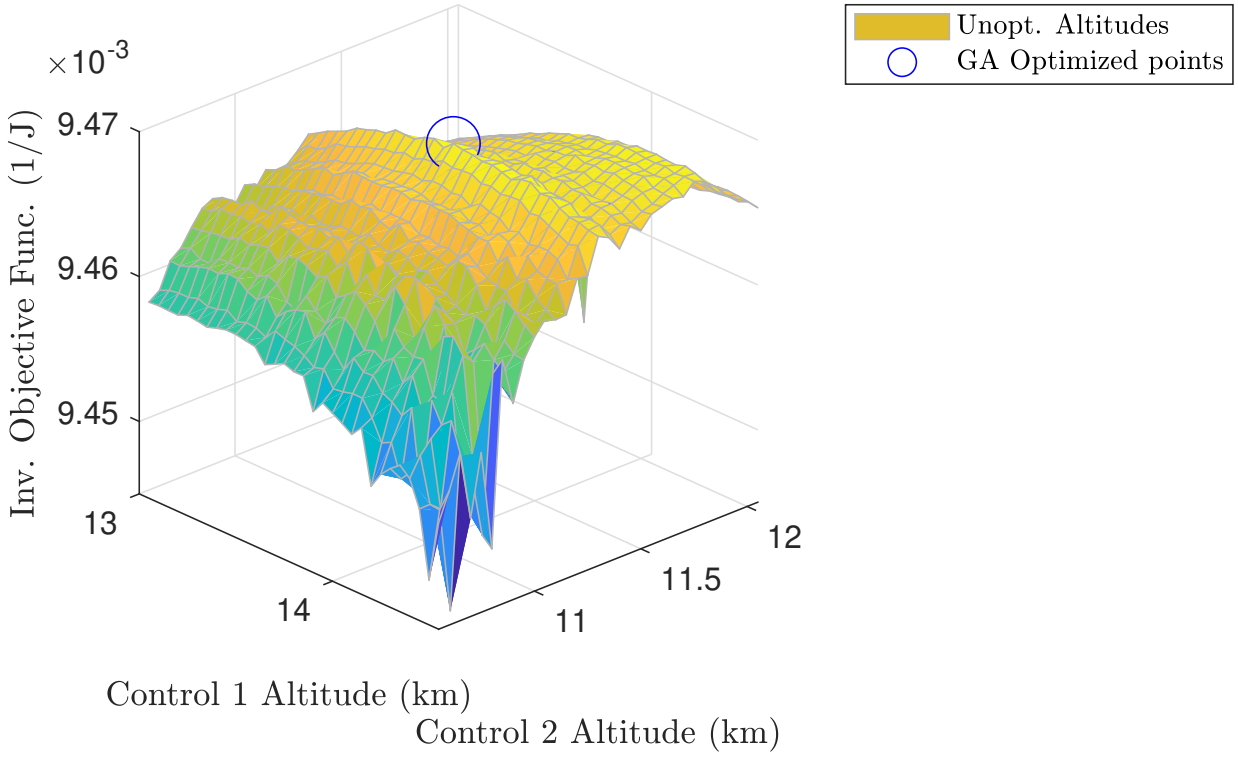

Figure 2.9: GA-validation case for two control points, h_{init}=8 km, M = 7.

In Figures 2.8 and 2.9, validation cases are presented for GA-optimized target trajectories for one and two control points, respectively. In both cases, the control variable was the altitude of points targeted by the HARV along the flight path for a ground target distance of 200 km. The one-point case optimized for target altitude at the 100 km downrange point, while the two-point case optimized for target altitudes at the 50 and 150 km downrange points ('Control 1' and 'Control 2', respectively in Figure 2.9). The solution points produced by the GA optimization are shown by the blue circle, and the surrounding data shows a sampling of the parameter space near the optimized point. The genetic algorithm was able to successfully find the global minimum in both instances (the inverse of the objective function is given in Figure 2.9 to increase clarity, so the optimal solution is the maximum instead of the minimum of the surface). These results supported the approach of using genetic algorithms for higher-dimension control variables, and ensuing optimization runs accounted for as many as nine control points, though computational time significantly increased, and convergence to the global optimum became less certain.

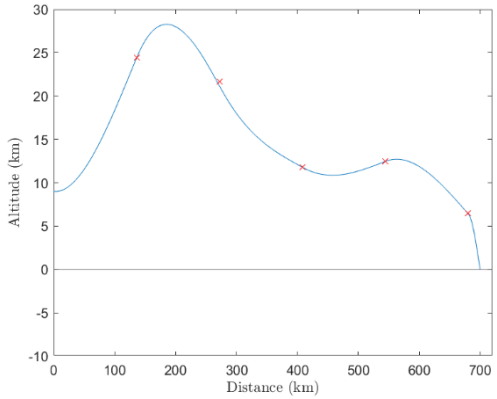

(a) 3rd generation fastest trajectory

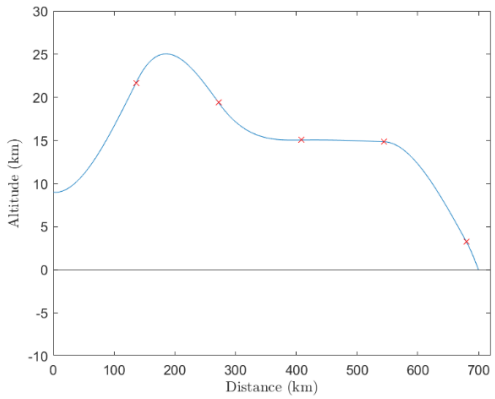

(b) 15th generation fastest trajectory

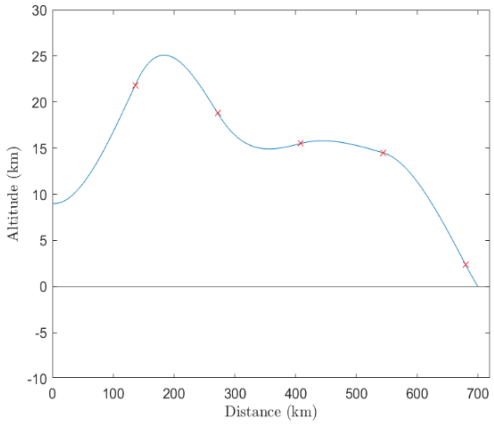

(c) 100th generation fastest trajectory

Figure 2.10: Best-trajectory progression of five control points for a Mach 7, 9 km launch, aimed at a 700 km downrange ground target

Table 2.3: Genetic algorithm progression outputs

Generation	Min time-to-target (s)
3	462.57
15	453.20
100	452.77

Figure 2.10 depicts an example of how the genetic algorithm improves flight time for a particular case over 3, 15, and 100 generations. Here, altitudes of five control points are used as control variables, depicted in the trajectories as red x's. While as many as 40 trajectories are evaluated for each generation, only the best-scoring trajectory from each generation is shown.

The total flight time of these best trajectories are given in Table 2.3. The early 3rd generation trajectory is considerable slower than the latter trajectories, but even at this early stage in the optimization process the general shape is well defined and the strike itself is accurate (all of the trajectories above impacted well within one meter of the target). After additional populations are evaluated, the 15th generation's best trajectory featured a slightly smaller initial pitch-up and a smoother mid-stage of the trajectory, which improved flight time by a little over nine seconds. Solution progression then slowed down somewhat, as after an additional 85 generations, only about 0.5 seconds of improvement could be found, and the 100th generation's best trajectory is highly similar in shape to that of the 15th generation.

This general pattern was seen throughout most trajectory optimization applications. As it was known that the genetic algorithm was not guaranteed to converge to a local or global optimum, algorithm settings were changed such that if an optimization run had not found a more optimal solution after 40 generations, optimization was terminated, and the solution was considered to be converged. In practice, this allowed for solving several different trajectories at different initial launch and target conditions in relatively short amounts of time, though in extreme cases optization runs could still take over an hour to complete.

Chapter 3: Results

3.1 Introduction

The following sections exhibit the finalized aerodynamic force database, as well as its use in subsequent trajectory simulation and optimization efforts. Lift, drag, moment, and lift-to-drag ratio curves are presented for the inviscid database, and sample drag curves are presented for the viscous database to exhibit the effect of changing Reynolds number. Trajectory results exhibit sample maximum range and optimized trajectories, as well as flight condition output data, viscous/inviscid trajtecory comparisons, physical reasonings for optimal trajectory shapes, and control point convergence studies.

3.2 HARV Aero Database

The following result from the simulation, post-processing, and parameter-space interpolation processes outlined in Section 2.2.

In Figures 3.1a and 3.1b, the fully developed inviscid drag and lift curves of the HARV are presented from α=-10° to +10° and from Mach numbers of 2 to 10. The simulation data is highlighted by the colored lines with symbols at each case, while the extrapolated data is shown by the black dotted lines. The overall trend with increasing Mach number is shown to be a

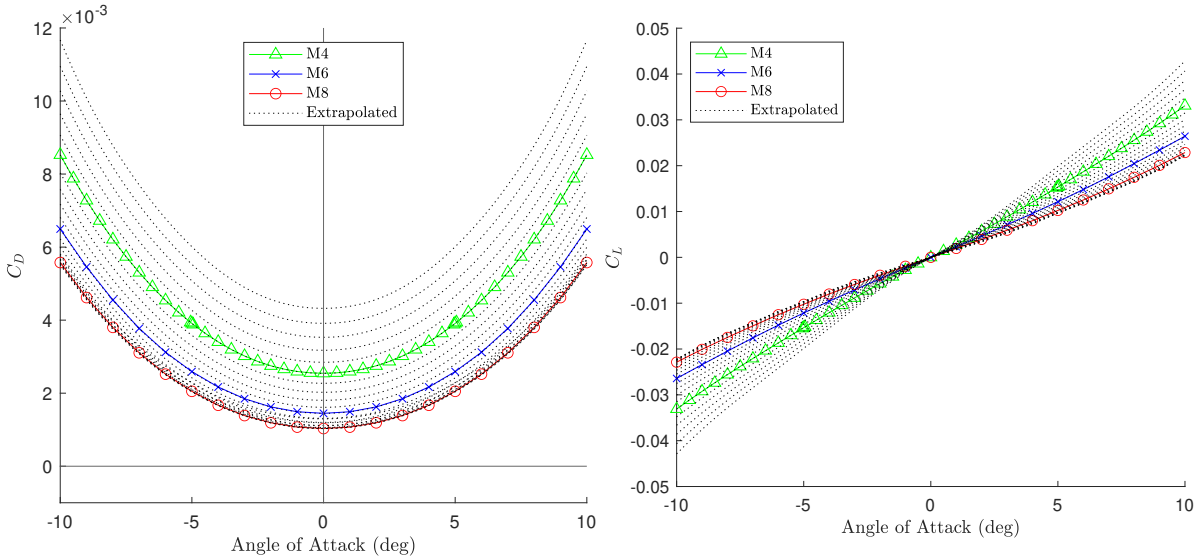

(a) HARV drag curve

(b) HARV lift curve

Figure 3.1: Inviscid lift and drag curves, measured and extrapolated data

decrease in both drag and lift coefficient, which is consistent with previous studies and governing theory. The interpolations were only based on simulations from three Mach conditions, so data is compressed towards the upper Mach range, with Mach 10 coefficients being almost equal to Mach 8 measured coefficients. At the lower Mach range, coefficient values are more spread out, with the delimeter Mach 2 data noticeably farther away from that of the measured Mach 4 cases. This trend also agrees well with theory, but it perhaps likely over-exaggerated by a low-dimension Mach simulation sample. The accuracy could likely be improved with the addition of simulated cases at the upper and lower ends of the already simulated cases (e.g. Mach 9 and Mach 3 cases).

A further note is that at the upper Mach range, velocities are such that real-gas phenomena such as vibrational excitation and intitial stages of Oxygen dissociation are present, depending on the local speed of sound and atmospheric density. This would mean that a calorically perfect gas assumption would begin to break down in this range, and that real-gas corrections would begin to be necessary in order to ensure more accurate estimations of flow conditions around the HARV

and the resulting aerodynamic forces. For this reason, the majority of flight simulations were performed with initial Mach numbers of 8 or lower.

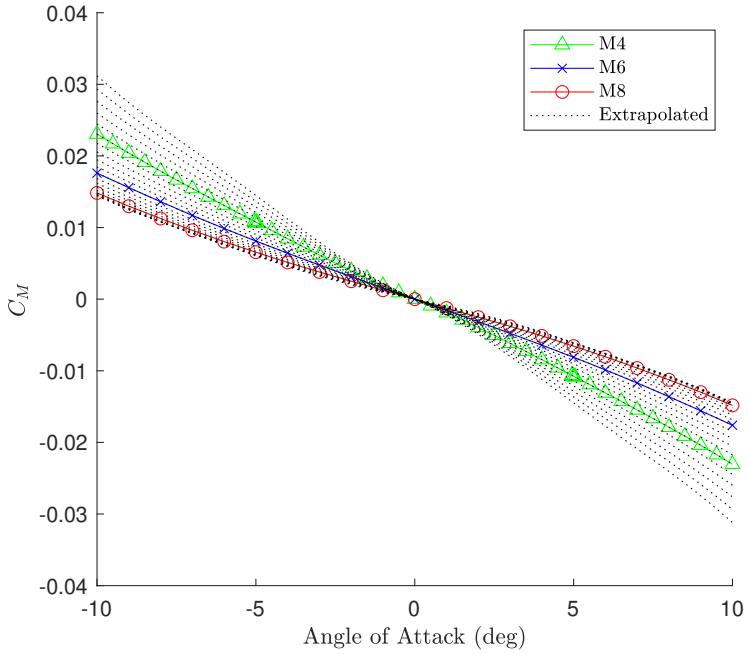

Figure 3.2: HARV moment coefficient, measured and interpolated data.

Figure 3.2 depicts the inviscid moment coefficient curve of the HARV, with moments measured about the center of mass. Once again, the observed trends in Mach-dependence agree well with expected results, with the slope of C_M with alpha becoming less pronounced as Mach is increased. The slope of the curve at all Mach numbers indicates that the HARV exhibits static longitudinal stability. A positive angle of attack produces a negative, pitch down moment, and a negative angle of attack yeilds a positive, pitch-up moment, which would both drive the HARV back towards zero if uncorrected by flight controls. A more in-depth stability derivative investigation effort would be needed to determine if the vehicle exhibits dynamic longitudinal stability at each Mach number.

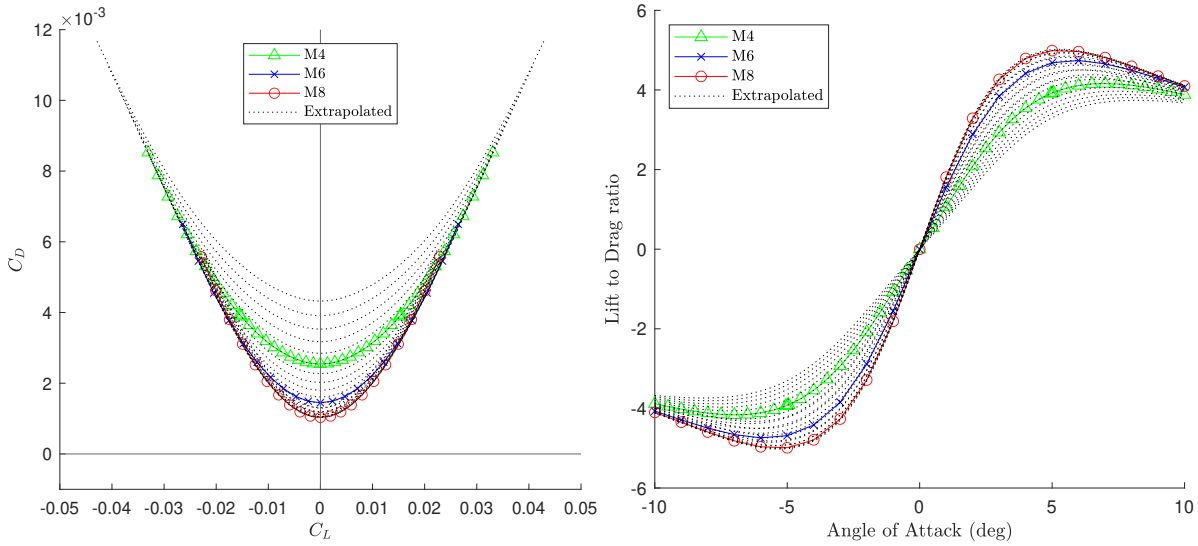

(a) C_D vs. Cc_L (b) L/D ratio vs. α

Figure 3.3: Inviscid drag polar and L/D ratio curves

The drag polars and L/D ratio curves are depicted in Figures 3.3a and 3.3b, respectively. The drag polar shows the effect of Mach on drag to be most pronounced at low-lift conditions. In the L/D ratio curve, maximum L/D ratio increases with an increase in Mach, and the angle of attack at which L/D_{max} occurs shifts to a lower angle of attack. This trend is notable, since it dictated a change in commanded α for the exploratory maximum range trajectory cases.

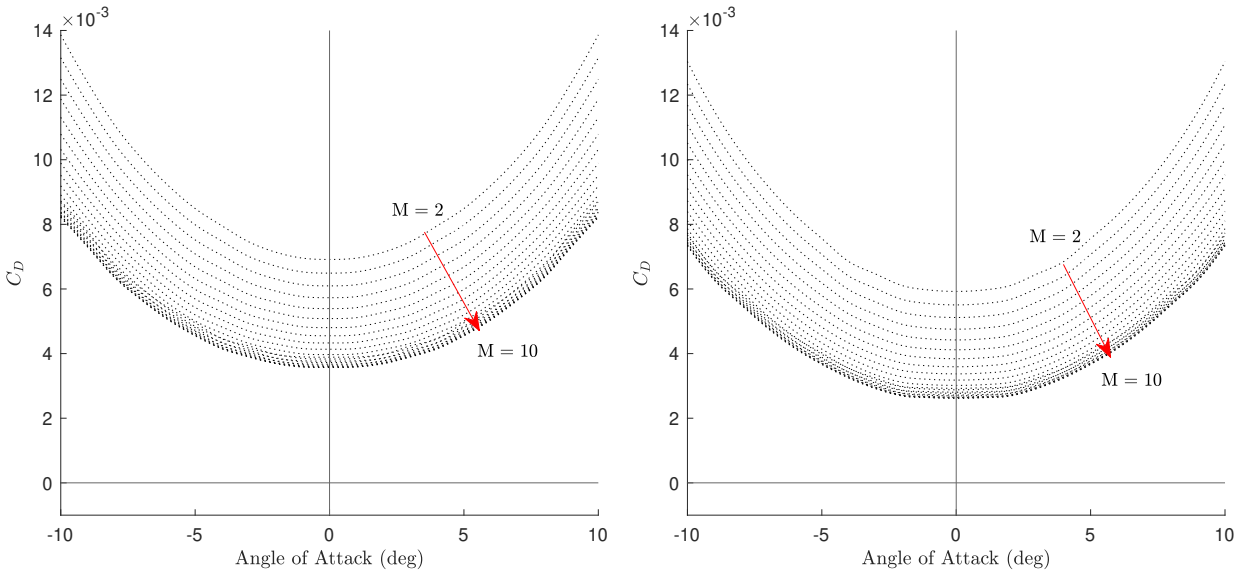

(a) $Re = 9 \times 10^6$ (b) $Re = 1.9 \times 10^8$

Figure 3.4: HARV viscous drag polors at varying Re

Figure 3.4 depicts sample drag polars from the viscous HARV database at relatively low and high Reynolds numbers. Again, drag coefficient is depicted as a function of alpha and Mach in each case. The shift upward in drag coefficient with a decrease in Reynolds number is consistent with governing theory.

Overall, this effort succeeded in constructing the HARV inviscid and viscous aerodynamic databases. By establishing coefficient relationships with respect to Mach, Reynolds number, and angle of attack, forces and resulting accelerations could be extracted for any given flight condition within the fairly generous parameter range. Careful formatting and discrete parameter-value storage was used in order to maximize their accessibility in the ensuing flight simulations and trajectory optimizations.

3.3 Trajectory Optimization

Maximum range trajectory simulations are shown as a basic application of the trajectory code, which are followed by comparisons of various time-optimized groundstrike trajectories. As a point of comparison, a straight-to-target trajectory is simulated to contrast the resulting cumulative drag impulses with those of optimized trajectories. Viscous and inviscid optimal trajectories are compared, and a control point convergence study is presented.

3.3.1 Maximum Range Results

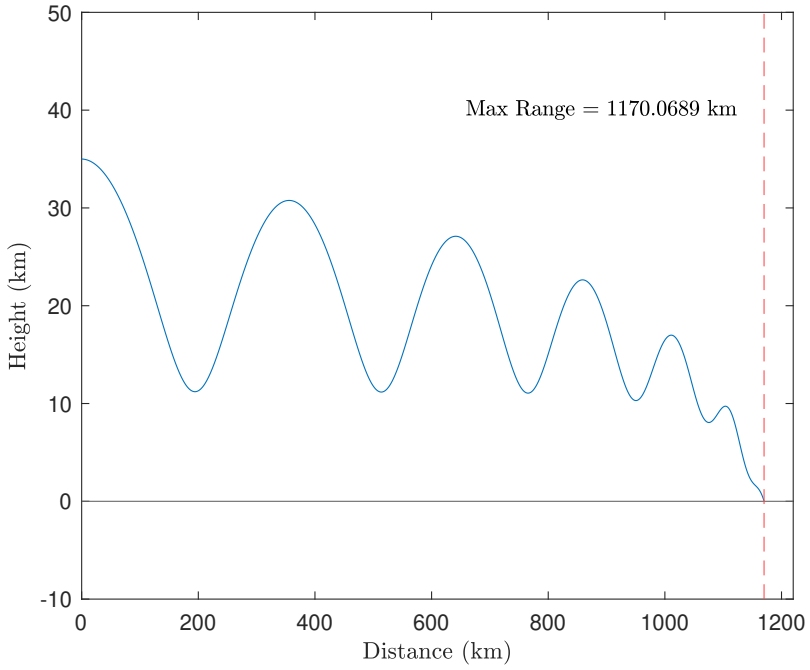

Figure 3.5: Max L/D trajectory, h_{init}= 35 km, M_{init} = 7.

To verify the HARV flight simulation code, a relatively simple algorithm was developed to fly a trajectory for which the angle of attack for maximum lift to drag ratio was tracked over the course of the flight. For a gliding vehicle, flying at $\alpha|_{L/Dmax}$ will always provide the

maximum glide range [17]. As previously discussed, the angle of attack at which max L/D occurs increases as Mach decreases. An example trajectory is provided in Figure 3.5, for which the initial conditions were an altitude of 35 km, a release angle of $0°$, and an initial Mach number of 7, corresponding to an initial velocity of 2,381 m/s. The load factor η expressed as a multiple of gravitational acceleration is shown in Figure 3.6.

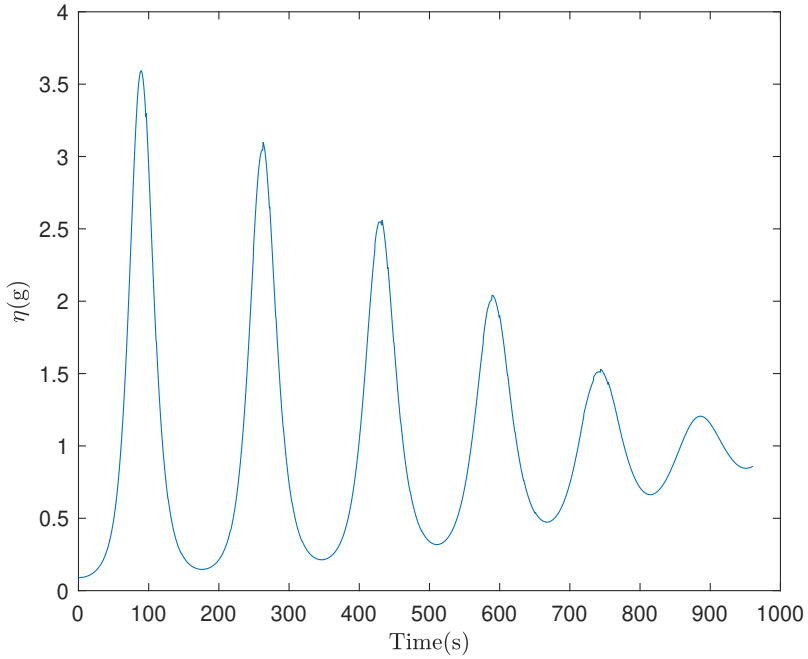

Figure 3.6: Max range load factor, h_{init}= 35 km, M_{init} = 7.

The sample trajectory exhibits the oscillarory flight path characteristic of high-lift hypersonic vehicles when in an unconstrained reentry phase [18]. At high altitude, the lift generated by flying at $\alpha|_{L/Dmax}$ is insufficient to maintain level flight. The HARV begins to descend and atmospheric density gradually increases, as does the nominal lift force. Eventually, the increase in lift is sufficient enough to reverse the descent and propel the HARV back to a higher altitude. The lift decays once again with a decrease in free-stream density, and the oscillitory flight path repeats with decreasing amplitude as velocity gradually bleeds off. If uncorrected, these oscillations can lead to high-intensity peak heating and structural loading, though in this particular case the

resulting g-loads are relatively mild, with the peak load being approximately 3.5 g's.

3.3.2 Minimized Time-to-Target Trajectories

Utilizing the previously described approach combining the PN controller and GA optimization, a selection of time and accuracy-optimized trajectories were produced and are presented here.

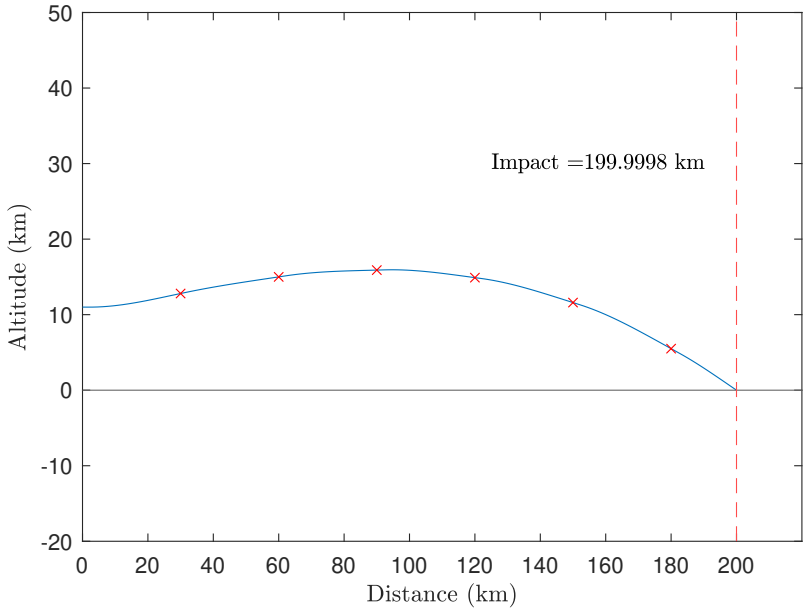

Figure 3.7: GA-optimized trajectory, h_{init}= 11 km, M_{init} = 7, $\theta_{init} = 0°$

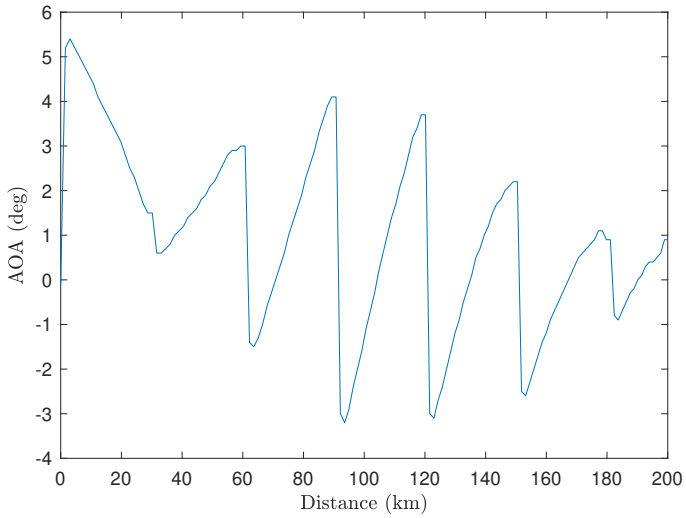

Figure 3.8: PN Controller α output, h_{init}= 11 km, M_{init} = 7.

Figures 3.7 and 3.8 depict an example of an optimized trajectory and the corresponding PN controller output. In this example, the altitudes of six equally-spaced control points are optimized to produce an accurate strike with minimal flight time. The optimized control points are depicted along the trajectory as an 'x'. One of the defining characteristics of this solution, as with most, was the immediate pitch-up maneuver, which resulted in the majority of the trajectory residing in the tropopause/lower stratosphere (nominally above 11 km). Consequently, the HARV benefited from a significant reduction in atmospheric density and resulting drag. Notably, however, the trajectory did not call for a pitch into the mid to upper-stratosphere, of which it was more than capable given its initial energy state. Despite the availability of further reduced density and drag at these higher altitudes, a balance was struck between the sustaining forward, closing velocity while significantly reducing net drag effect.

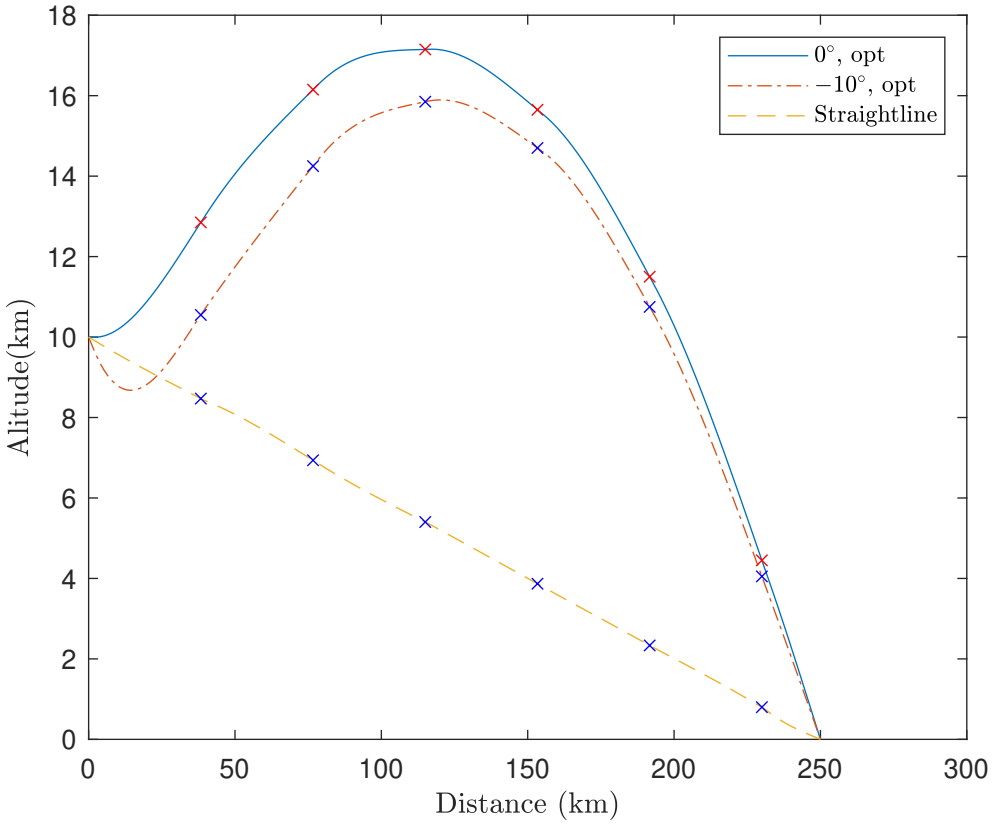

Figure 3.9: Optimized vs. 'straightline' trajectory comparison.

Table 3.1: Optimal and straightline flight times.

Trajectory	t_{flight} (s)
Optimal, 0°	158.90
Optimal, -10°	166.39
Straightline	174.08

As a means of verifying that the genetic algorithm was not finding solutions that were biased, optimal cases were flown at launch angles of zero and -10 degrees, and a basic 'straightline' path was constructed as a point of comparison. The results are shown in Figure 3.9 and Table 3.1. As shown, both of the optimal, altitude-seeking trajectories outperformed the straighline trajectory by several seconds. This is a particularly demonstrative case of the benefit gained from flying high for longer, even at the expense of performing a high-drag pitch up maneuver at the onset of the trajectory, such as in the case of the optimized case with a -10° launch release angle.

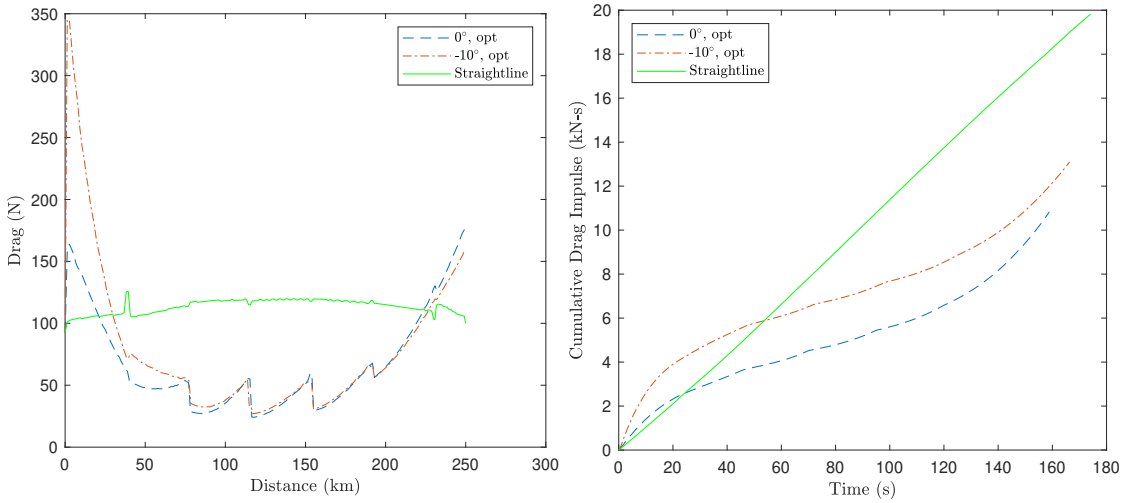

(a) Drag vs. distance

(b) Cumulative drag impulse vs. time

Figure 3.10: Optimized and straightline trajectory drag profiles

Figures 3.10a and 3.10b further illustrate the benefit of low-density altitude seeking trajectories. Figure 3.10a shows the free-stream relative drag over the downrange distance of each trajectory,

while Figure 3.10b shows the time-integrated cumulative drag impulse against the time of each trajectory. Clearly, each of the optimized trajectories suffers an increase in instantaneous drag from the pitch-up maneuver commanded immediately upon release, differing from the straightline trajectory which shows a fairly consistent resultant drag over the entire course of the flight. However, this benefit is short-lived, as the net effect of drag is matched by the optimal trajectories by approximately the 25 and 50 second marks for the 0° and -10° trajectories, respectively. The cumulative drag impulse then remains much lower for the remainder of the flight in both optimal cases, as compared to the straight trajectory baseline. Furthermore, the instantaneous drag of the optimal cases only subsequently exceeds that of the straightline trajectory during the last 25 km of the flight, as they encounter the denser, lower layers of the atmosphere at a higher speed than the same span in the straightline case. Mission planners working on platforms similar to the HARV should therefore highly prioritize operating in a high-altitude glide/subsequent dive flight mode when trying to minimize time to target, as opposed to opting for a more direct route which would lead to spending more of the flight in tropospheric altitudes and suffering from the detrimental impact on cumulative drag.

In Figure 3.11 below, a comparison is shown between an optimized inviscid trajectory, an optimized viscous trajectory, and a viscous trajectory flown using the inviscidly-optimized control inputs. In these optimization cases, angle of attack is controlled directly during discrete sections of the trajectory, though a PN-controller is still used during the terminal phase of the flight. These cases demonstrate the effect of including viscous corrections on the resulting trajectory shape and time. The optimal inviscid trajectory had a flight time of 105.6 seconds, while the optimal viscous trajectory had a flight time of around 111.3 seconds.

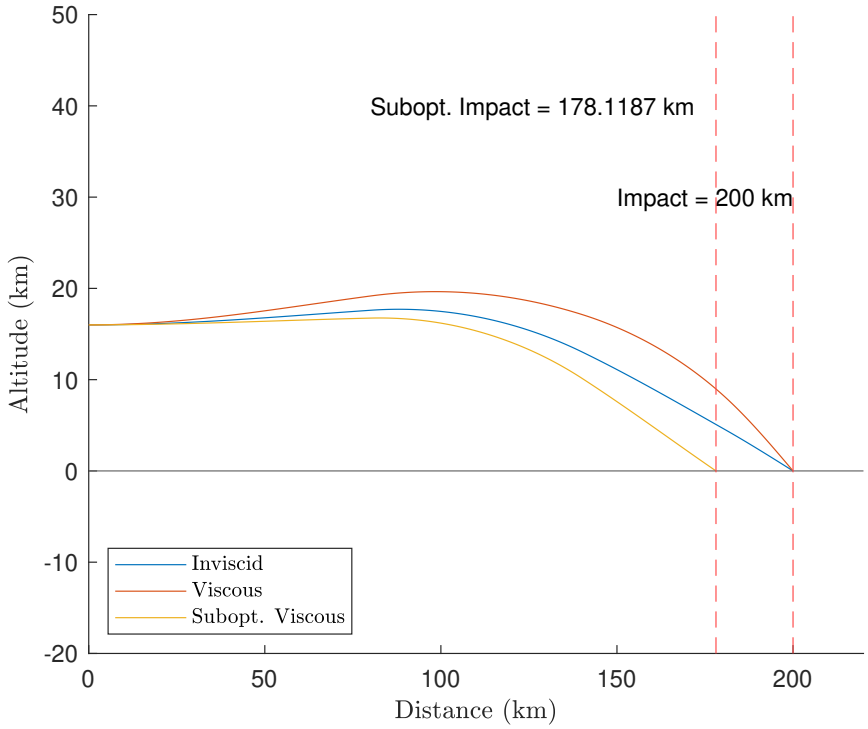

Figure 3.11: Inviscid/Viscous direct-alpha trajectory comparison

Because the benefit of achieving higher altitude is compounded by the introduction of a Reynolds number dependence for drag, the optimized viscous trajectory initially commands a higher angle of attack compared to the optimized inviscid trajectory, and subsequently compensated with a more negative angle of attack during the latter portion of the flight in order to align more directly to the target. When the inviscidly-optimized alpha profile is flown incorporating viscous effects, the HARV impacts the ground over 20 km short of the target distance, demonstrating the fairly substantial effect that viscous corrections can have on a given trajectory's success.

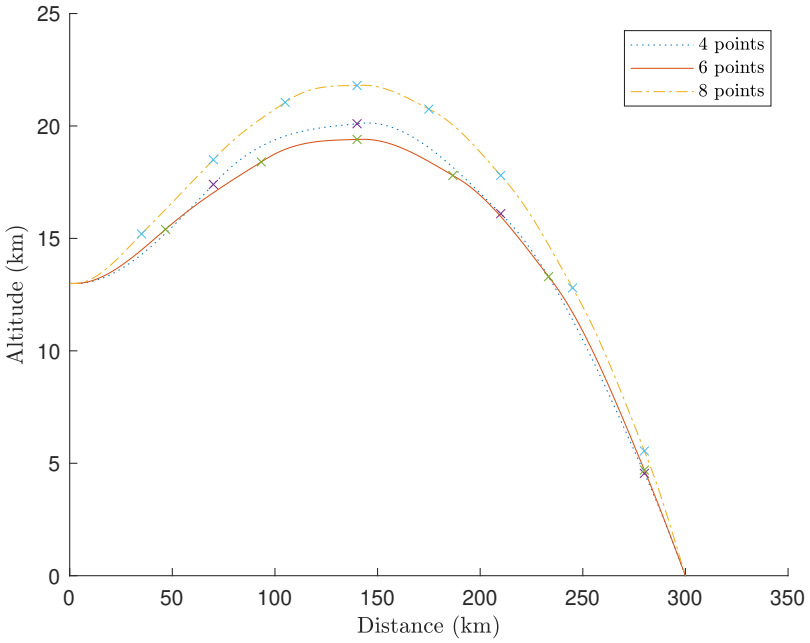

Figure 3.12: Varied control point dimension trajectories

Table 3.2: Control point dimension output comparison

Control points	t_{flight} (s)	Func. Count
4	162.06	2,664
6	162.04	6,846
8	162.49	31,548

Figure 3.12 shows three trajectories for the same initial conditions (M = 7, h_{init}=13 km) with control point dimensions of 4, 6, and 8, and Table 3.2 gives their final flight times and the number of function counts required by the genetic algorithm to reach psuedo-convergence. As evidenced by the overall poorer performance by the eight control point trajectory, there is a limit in this implementation to the amount of control points it is possible to add before efficiency significantly deteriorates and the possibility for optimization stalling arises. An increased control point dimension led to an increase in evaluations required for each generation, as the ways in which solutions could be mutated or crossed over with other solutions was compounded. This led

to an increase in runtime for each generation, and seemed to increase the amount of generations necessary to progress the solution closer to the true optimum. Either an inconveniently long optimization runtime or more fine-tuning of solver mutation parameters would be necessary to allow for an increase in the number of control points. Ultimately, it seems to be unnecessary. Although the four and six-point trajectories provide less overall spatial resolution on the target altitudes needed to achieve minimum time to target, and it is still unclear if they have actually arrived at a true local optimum, they are agreed to within two hundredths of a second on the optimal flight time, and boast a significantly reduced computational cost.

Chapter 4: Conclusions

The present work is an attempt at a CFD-derived construction of an aerodynamic database for the HARV, and subsequent use of that database in a trajectory optimization process. Inviscid CFD simulations of the HARV were performed at discrete Mach numbers over an angle of attack sweep. Post-processing treatment and base-pressure correction provided baseline values for lift, drag, and moment coefficient values. Integrated boundary layer corrections allowed for an efficient way to estimate viscous forces, and the results were subsequently interpolated and extrapolated across the Reynolds number, Mach, and angle of attack parameter spaces.

Once complete, the database was integrated with a Runge-Kutta based trajectory simulation code, a proportional-navigation controller logic, and a genetic-algorithm optimization method to characterize minimum-time groundstrike trajectories. The proportional-navigation controller was significant to drawing meaningful results from the study, as it allowed for the direct targeting of altitudes along the trajectory. Altitude control proved to be the dominant factor in optimal trajectory shape. A 'middle ground' of altitude was shown to be most efficient in reaching the target quickly, where the HARV was commanded to fly at altitudes which were high enough to experience a significant drag reduction but not attempt to fly unnecessarily high and thereby expend energy travelling vertically which could otherwise be used to close to the target more quickly. The cumulative drag benefit gained over more direct trajectories was observed and

was the most illuminating physical reasoning behind the characteristic shape of the optimized trajectories.

Although lacking in efficiency, use of genetic algorithms proved to be capable of approximating the shape of time-optimized groundstrike trajectories to a reasonable degree. Convergence to globally optimal trajectories was not achieved, but the relatively low control point-dimension approach combined with the use of a flight controller provided a solid basis for more sophisticated and real world control-oriented optimization approaches. The key conclusions from this effort are summarized as:

1. Aerodynamic databases, defined across adequately wide parameter spaces, are an efficient way of modelling flight dynamics of hypersonic vehicles, and eliminate the need for complex force calculations over the wide range of encountered flight conditions.

2. The fastest groundstrike trajectories for high-speed payload-oriented platform such as the HARV are those which achieve or maintain super-tropospheric altitudes until the final phase of flight, but do not fly so high as to overly-penalize closure rate to the target.

3. Viscous effects have a considerable impact on both the overall shape and expected flight time of minimized-time strike trajectories, and generally point to vehicles such as the HARV needing to fly higher for longer than inviscid results might suggest.

4. Genetic algorithms are capable of finding near-optimal solutions to time-minimized groundstrike trajectories, but rely on careful problem formulation, control variable discretization, and solver parameter setup in order to avoid being exceedingly inefficient.

4.1 Recommendations for Future Work

There are a number of flight dynamics which are overlooked in the limited scope of this work. Firstly, the database does not account for any sort of unsteady effects, which would be necessary to incorporate in the case of a high-frequency commanded maneuver. Implementation of the PN controller logic led to very few instances of steady-state angle of attack inputs, and some fairly large angle of attack jumps, which introduces a degree of uncertainty in the final trajectory results. To correct for this, methods such as piston theory could be incorporated into the database to be used to approximate unsteady coefficient values during maneuvers of a relevant pitch rate.

Secondly, a perfect gas assumption has been used as a proxy for incorporating real-gas effects, which are especially relevant at high-enthalpy flight states. As previously stated, real gases at upper limits of the database used here (Mach 10) would begin to encounter Oxygen dissociation depending on the atmospheric conditions, which would result in forces varying significantly from those derived from a calorically perfect gas assumption. The database could potentially be re-constructed using real gas models in the CFD simulations to explore if there is a change in trajectory characteristics when including these effects, or another surrogate model could be used to modify perfect gas-derived values only when necessary.

Another potential addition to the database to add realism would be to model control surfaces of the HARV, and re-run trajectories at at various control deflection angles to determine ”trimmed” coefficient values. This would involve first determining the moment produced by the HARV at a given angle of attack, before determining the flight control deflecttion angle necessary to cancel out that moment and hold an angle of attack, and finally re-solving for the resulting lift and

drag forces at that α and control state. Control surface dependence could be integrated with the proportional navigation controller or an alternative logic to significantly augment the realism of the simulations being performed. It is further recommended that practical constraints of interest be added to the optimized trajectory solutions, including limiting the peak heating, load factor, minimum dynamic pressure necessary to provide effective control surfaces, and including ”no-fly” zones or interception avoidance behavior to better model adversary-influenced real-world trajectories.

Although the optimization efforts here focused only on minimizing time to target, several other constraints of interest could be incorporated in order to provide more mission-specific optimal trajectories. Including constraints on peak heating or aerodynamic force could reveal some of the optimal trajectories presented here to be structurally unrealistic, and demonstrate how trajectories would need to be changed in order to avoid having to change the design limits of the HARV and similar vehicles. Should control surfaces be implemented, a study could be performed to determine the minimum dynamic pressure necessary to maintain positive control authority, which would provide an additional constraint to add realism. Additionally, the implementation of ’no-fly zones’ and other adversarial considerations could explore the ability of the HARV to avoid potentially mission-hazardous areas or intercept vehicles.

Finally, the use of genetic algorithms, while not entirely disadvantageous for previously outlined reasons, could benefit from the use of offline ”training” to improve solution convergence time. This could either be accomplished by an iterative constriction on the control variable space based on previous results, or, to build upon an approach developed by Shi and Wang [5], by the use of neural networks outside of the genetic algorithm loop.

Appendix

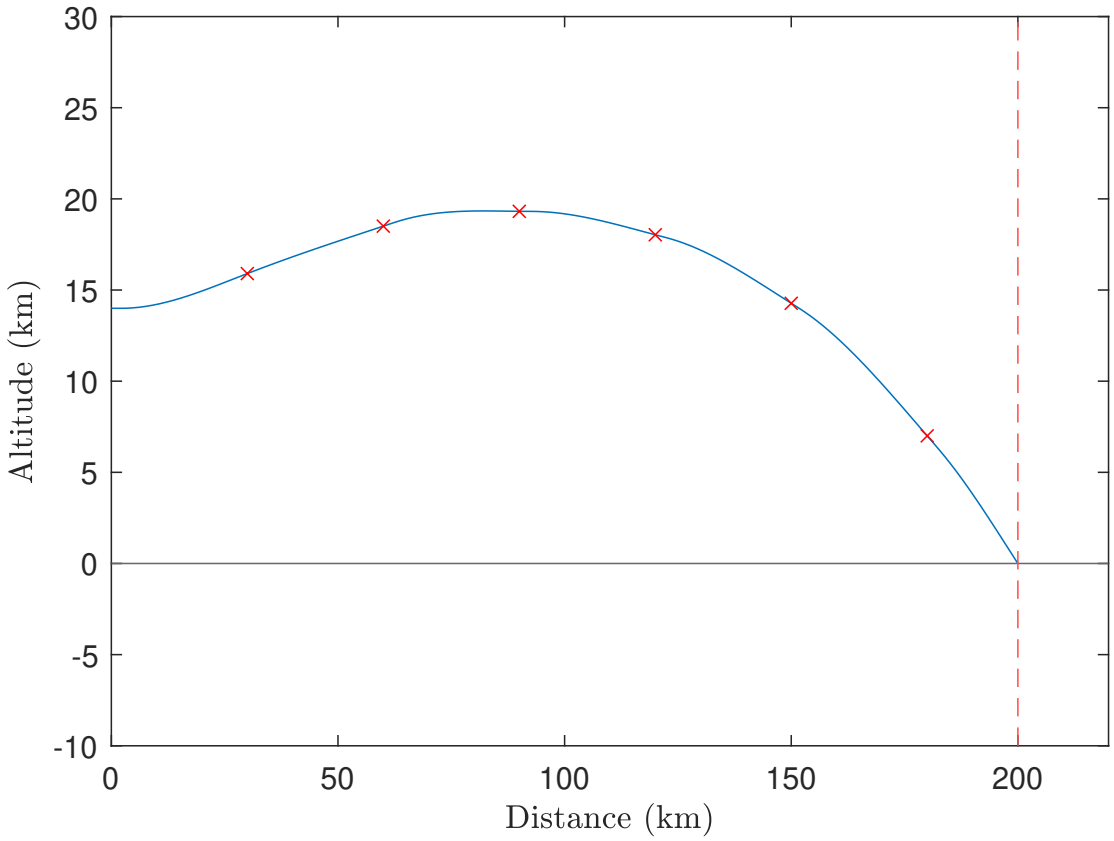

Figure 4.1: Single trajectory example, h_{init} = 14 km, M_{init} = 7

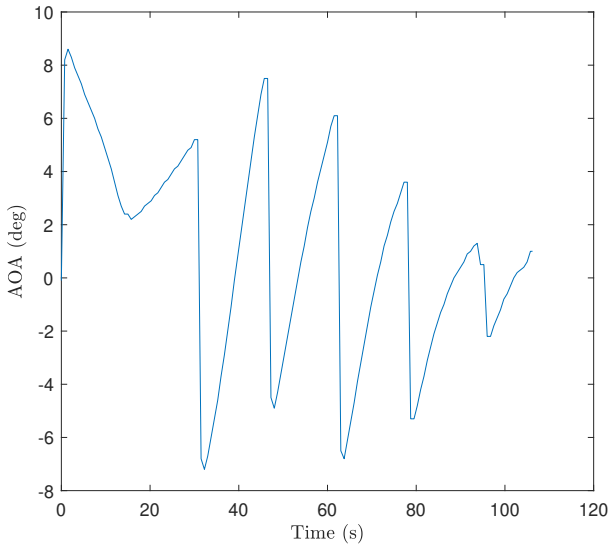

(a) AOA vs. time

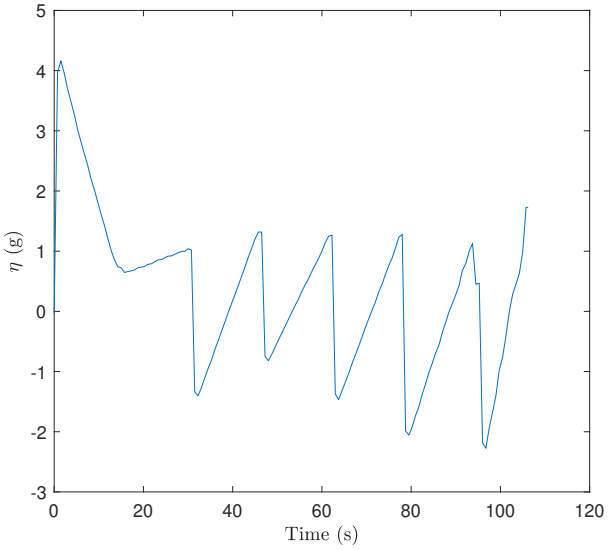

(b) Load factor vs. time

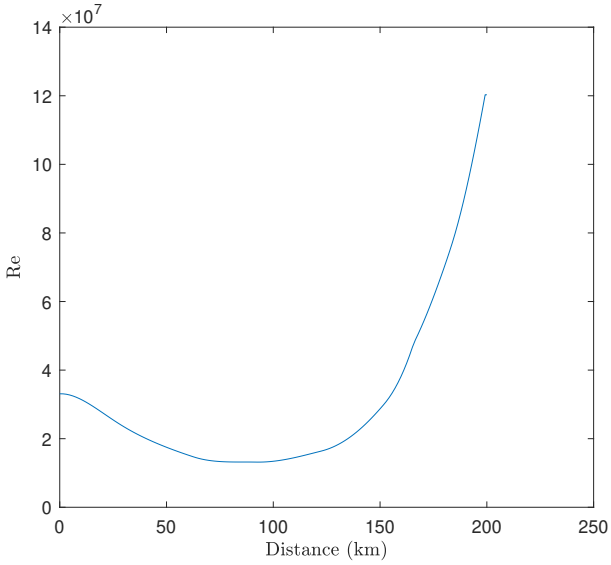

(c) Re vs. distance

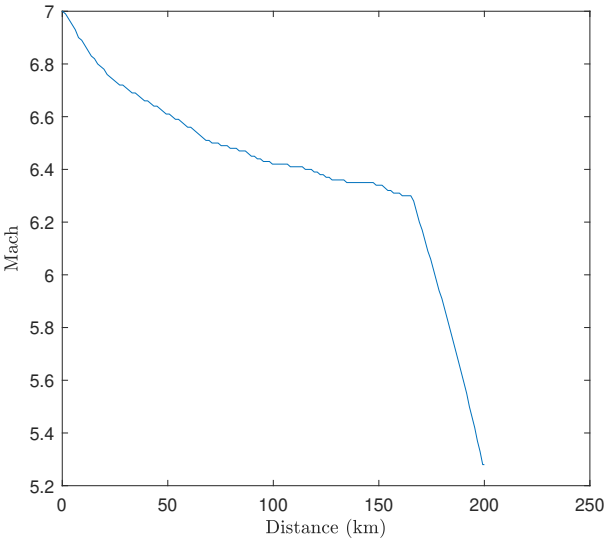

(d) Mach vs. distance

Figure 4.2: Flight data from trajectory in Figure 4.1

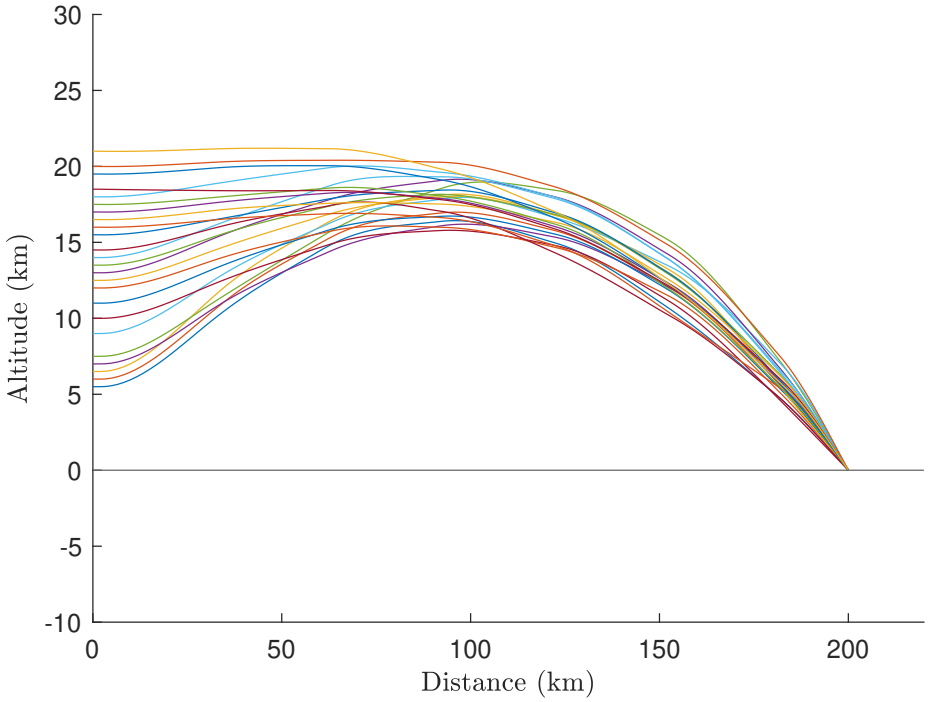

Figure 4.3: Mach 7 trajectories with varied initial altitude

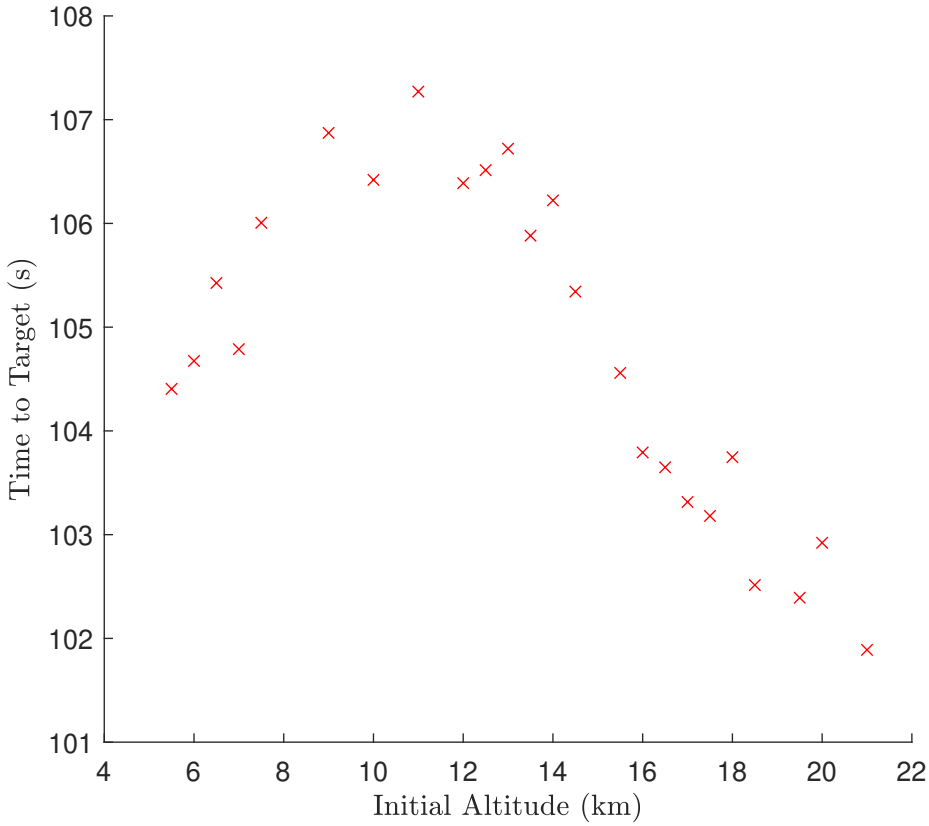

Figure 4.4: Time to target vs. Initial Altitude, Mach 7

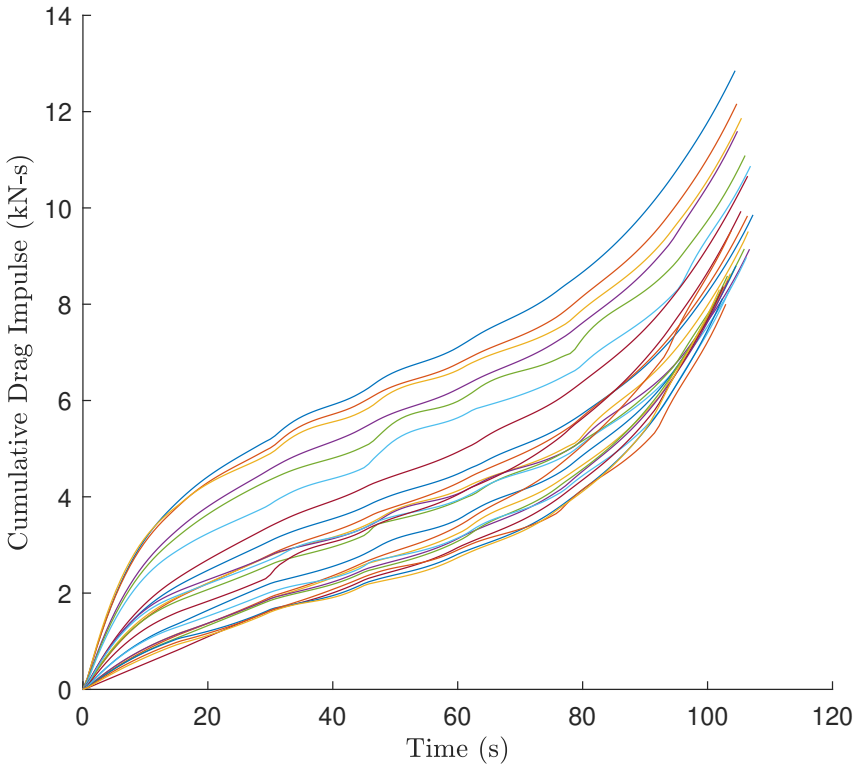

Figure 4.5: Cumulative drag-impulse, trajectories from Figure 4.3

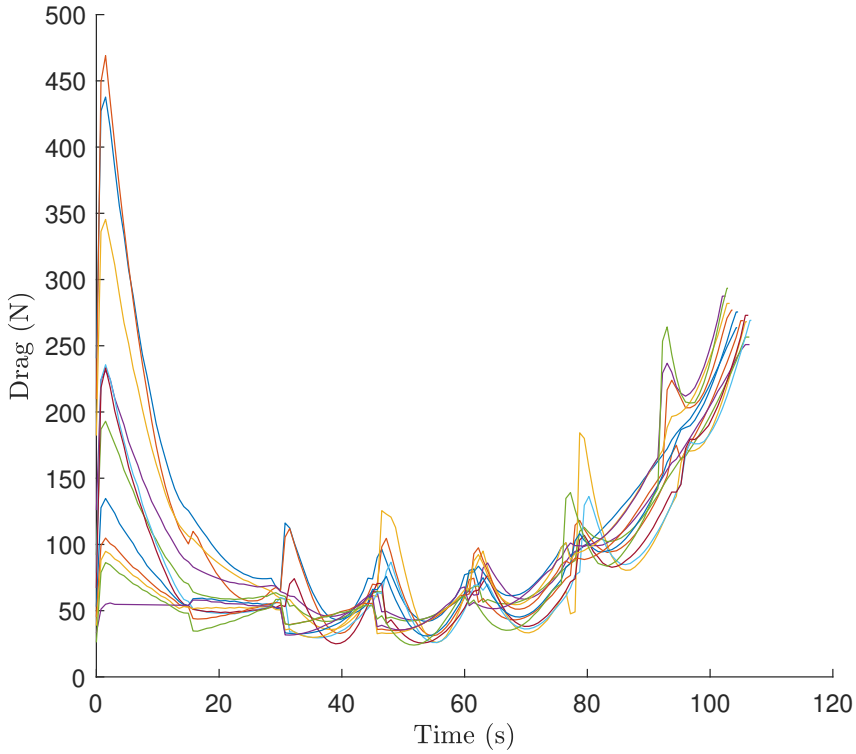

Figure 4.6: Instantaneous drag vs. time, trajectories from Figure 4.3

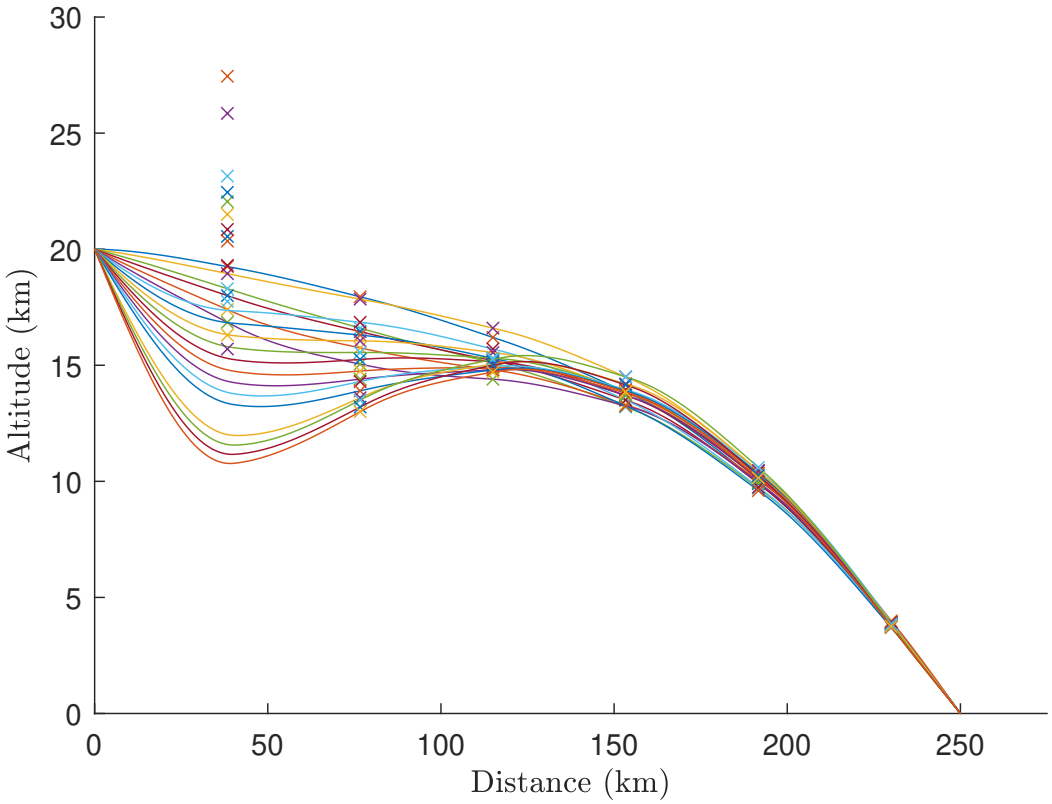

Figure 4.7: Mach 6 trajectories, varied release angle

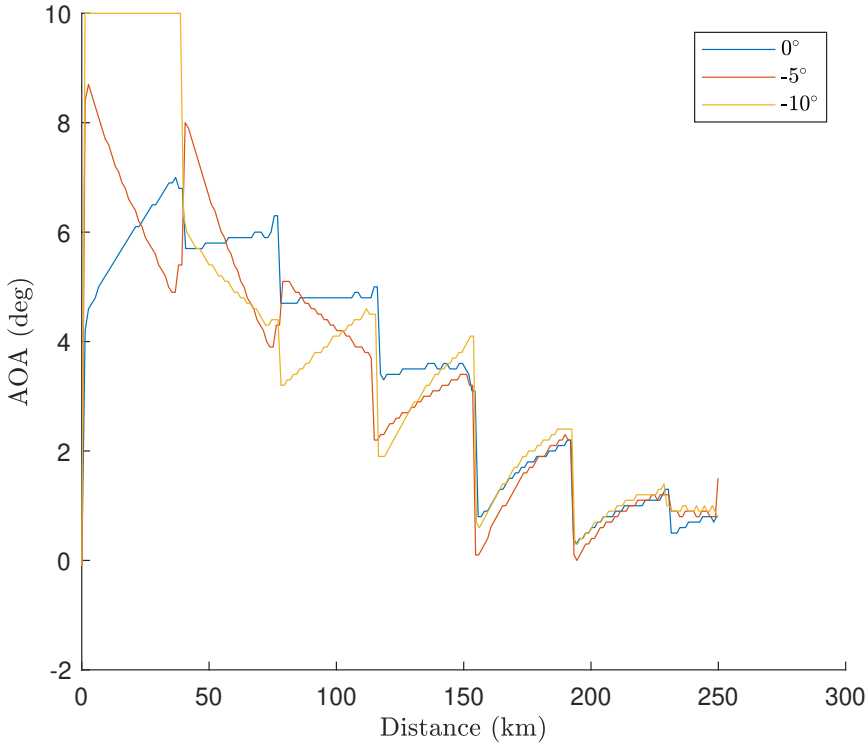

Figure 4.8: Varied release angle AOA outputs

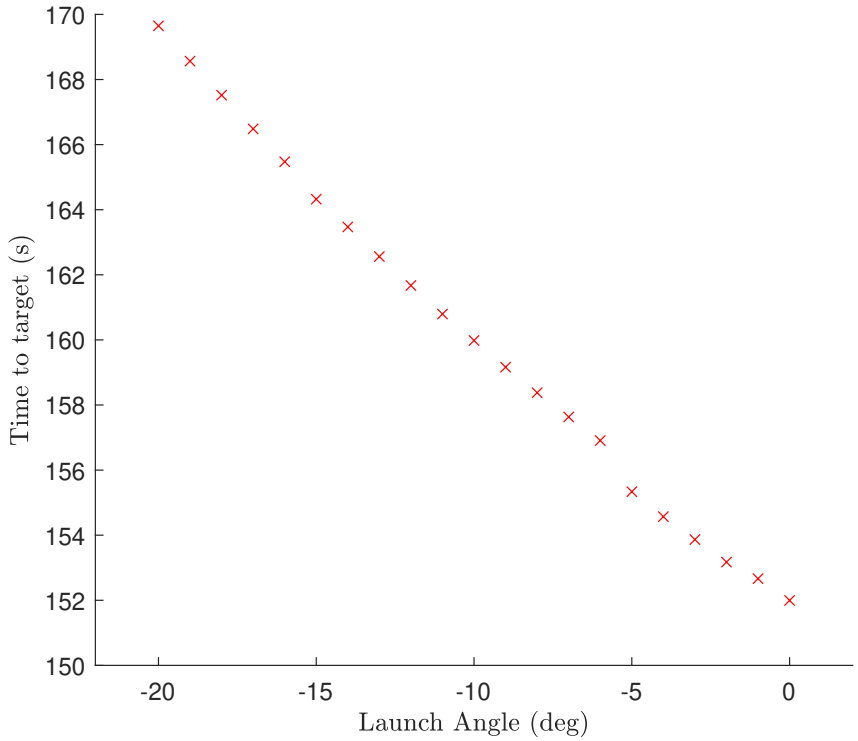

Figure 4.9: Time to target vs. release angle from trajectories in Figure 4.7

Bibliography

[1] Raymer, D. P., “Aircraft Design: A Conceptual Approach,” *AIAA Education Series*, Reston, VA, 2018.

[2] Anderson, J. D., ”Hypersonic and High-Temperature Gas Dynamics”, *American Institute of Aeronautics and Astronautics*, 2019; pages 15-32

[3] J. D. Vasile et. al, ”High-Speed Army Reference Vehicle” *DEVCOM Army Research Laboratory*, August 2022.

[4] Pamadi, B., Brauckman, G. et. al., ”Aerodynamic Characteristics, Database Development and Flight Simulation of the X-34 Vehicle”, *Journal of Spacecraft and Rockets*, Vol. 38, No.3, May 2001.

[5] Shi, Y. and Wang, Z., ”A Deep Learning-Based Approach to Real-Time Trajectory Optimization for Hypersonic Vehicles”, *AIAA Scitech Forum*, 2020.

[6] Pamadi, B., Pei, J., Covell, P., Favaregh, N., Gumbert, C., and Hanke, J., “Aerodynamic Analyses and Database Development for Lift-Off/Transition and First Stage Ascent of the Ares I A106 Vehicle,” *49th AIAA Aerospace Sciences Meeting including the New Horizons Forum and Aerospace Exposition*, 2011. https://doi.org/10.2514/6.2011-12

[7] Rizzi, A., Goetzendorf-Grabowski, T., Vos, J., Mieszalski, D., Ronch, A. D., Tomac, M., and Ghoreyshi, M., "Creating Aero-Databases by Adaptive-Fidelity CFD Coupled with S&C Analysis to Predict Flying Qualities," *CEAS European Air & Space Conference*, Manchester, 2009.

[8] McCarthy, K., "The JSF STOVL Performance Process from Small-Scale Database to Flight Test Demonstration," 2002 Biennial International Powered Lift Conference and Exhibit, American Institute of Aeronautics and Astronautics, 2002. https://doi.org/10.2514/6.2002-6002

[9] Jorris, T. R., and Cobb, R. G., "Three-Dimensional Trajectory Optimization Satisfying Waypoint and No-Fly Zone Constraints," *Journal of Guidance, Control, and Dynamics*, Vol. 32, No. 2, 2009, pp. 551–572. https://doi.org/10.2514/1.37030

[10] Coulter, B., Wang, Z., Huang, D., and Yao, Y., "Hypersonic Trajectory Optimization with High-Fidelity Aerothermodynamic Models," *AIAA Scitech Forum*, 2021. https://doi.org/10.2514/6.2021-0715

[11] Wang, Z., and Grant, M. J., "Hypersonic Trajectory Optimization by Sequential Semidefinite Programming," *AIAA Atmospheric Flight Mechanics Conference*, 2017. https://doi.org/10.2514/6.2017-0248

[12] van Noordt, W., Ganju, S., and Brehm, C., "Immersed-Boundary Wall-Modeled Large-Eddy Simulation of High Mach Number Boundary Layer Flows," *AIAA AVIATION 2021 FORUM*, American Institute of Aeronautics and Astronautics, 2021. https://doi.org/10.2514/6.2021-2751

[13] Faruqi, F., "Integrated Navigation, Guidance, and Control of Missile Systems: 2-D Dynamic Models," *Australian Government Dept. of Defense, Defense Science and Technology Group*, September 2013.

[14] Siouris, G., "Missile Guidance and Control Systems," *Springer-Verlag*, New York, 2004. https://doi.org/10.1007/b97614

[15] Innocenti, M., Pollini, L., and Turra, D., "Guidance of Unmanned Air Vehicles Based on Fuzzy Sets and Fixed Waypoints," *Journal of Guidance, Control, and Dynamics*, Vol. 27, No. 4, 2004, pp. 715–720. https://doi.org/10.2514/1.2651

[16] Shapira, I., and Ben-Asher, J. Z., "Near-Optimal Horizontal Trajectories for Autonomous Air Vehicles," *Journal of Guidance, Control, and Dynamics*, Vol. 20, No. 4, 1997, pp. 735–741. https://doi.org/10.2514/2.4105

[17] Hurt, H. H., "Aerodynamics for Naval Aviators," *Federal Aviation Administration*, Renton, Wash, 1992.

[18] Lu, P., Forbes, S., and Baldwin, M., "Gliding Guidance of High L/D Hypersonic Vehicles," *AIAA Guidance, Navigation, and Control (GNC) Conference*, American Institute of Aeronautics and Astronautics, 2013. https://doi.org/10.2514/6.2013-4648

[19] Maxwell, J., *Morphing Waveriders for Atmospheric Entry*, Ph.D. Dissertation. University of Maryland, College Park, 2019.

[20] Grant, M. J., and Braun, R. D., "Rapid Indirect Trajectory Optimization for Conceptual Design of Hypersonic Missions," *Journal of Spacecraft and Rockets*, Vol. 52, No. 1, 2015, pp. 177–182. https://doi.org/10.2514/1.A32949

[21] Saranathan, H., and Grant, M. J., "Incorporation of Effects of Control Surfaces into Hypersonic Trajectory Optimization Framework," *AIAA Atmospheric Flight Mechanics Conference, American Institute of Aeronautics and Astronautics*, 2016. https://doi.org/10.2514/6.2016-3245

[22] Lomax, H., Pulliam, T. H., and Zingg, D. W., "Fundamentals of Computational Fluid Dynamics," *Springer*, New York, 2001.

[23] Shampine, L. F., and Reichelt, M. W., "The MATLAB ODE Suite," *SIAM Journal on Scientific Computing*, Vol. 18, No. 1, 1997, pp. 1–22. https://doi.org/10.1137/S1064827594276424

[24] "How the Genetic Algorithm Works - MATLAB & Simulink." Retrieved 29 November 2023. https://www.mathworks.com/help/gads/how-the-genetic-algorithm-works.html

[25] "Vary Mutation and Crossover - MATLAB & Simulink." Retrieved 2 December 2023. https://www.mathworks.com/help/gads/vary-mutation-and-crossover.html